Mechanism of alteration in passivity of additively manufactured Ni-Fe-Cr Alloy 718 caused by minor carbon variation

Arshad Yazdanpanah , Gioele Pagot , Mattia Franceschi , Pietro Rebesan , Mattia Venturin , Julia Botinha , Bodo Gerhmann , Iris De Graeve , Vito Di Noto , Reynier I. Revilla , Manuele Dabalà

PII: S0013-4686(24)01163-0
DOI: https://doi.org/10.1016/j.electacta.2024.144925
Reference: EA 144925

To appear in: *Electrochimica Acta*

Received date: 5 July 2024
Revised date: 1 August 2024
Accepted date: 18 August 2024

Please cite this article as: Arshad Yazdanpanah , Gioele Pagot , Mattia Franceschi , Pietro Rebesan , Mattia Venturin , Julia Botinha , Bodo Gerhmann , Iris De Graeve , Vito Di Noto , Reynier I. Revilla , Manuele Dabalà , Mechanism of alteration in passivity of additively manufactured Ni-Fe-Cr Alloy 718 caused by minor carbon variation, *Electrochimica Acta* (2024), doi: https://doi.org/10.1016/j.electacta.2024.144925

Mechanism of alteration in passivity of additively manufactured Ni-Fe-Cr Alloy 718 caused by minor carbon variation

Arshad Yazdanpanah[a]*, Gioele Pagot[a], Mattia Franceschi[b], Pietro Rebesan[c], Mattia Venturin[a], Julia Botinha[d], Bodo Gerhmann[d], Iris De Graeve[e], Vito Di Noto[a], Reynier I. Revilla[e]*, Manuele Dabalà[a]

[a] Department of Industrial Engineering, University of Padova, Via Marzolo 9, 35131 Padova, Italy

[b] Department of Engineering and Management, University of Padova, Stradella San Nicola 3, 36100 Vicenza, Italy

[c] National Institute for Nuclear Physics (INFN) Padova Division, Padova, Italy

[d] VDM Metals International GmbH, Kleffstraße 23, D 58762 Altena, Germany

[e] Vrije Universiteit Brussel, Department of Materials and Chemistry (MACH), Research Group Sustainable Materials engineering (SUME)

Corresponding authors: arshad.yazdanpanah@phd.unipd.it

rrevilla@vub.be

Abstract

Unlike conventional alloys, where carbon content typically promotes carbide compound formation and reduces localized corrosion resistance, the impact of carbon in additively manufactured materials remains largely unexplored due to rapid cooling rates inhibiting carbide formation. This study addresses the novel question of whether reducing carbon content benefits corrosion performance and its underlying mechanisms in Ni-Fe-Cr-based alloy 718. Employing high-resolution techniques and microcapillary electrochemical methods, it was revealed that higher carbon content increases dislocation density at cell boundaries. This increased dislocation density facilitates the enhanced ejection of nickel and iron from the protective chromium oxide layer on the surface, leading to the formation of a defective outer Ni-Fe oxide layer. This compromised layer subsequently diminishes the alloy's corrosion resistance, particularly under tensile stress conditions.

Keywords: Metal additive manufacturing; Ni-Cr-based alloy; Corrosion; Passivity; semiconducting behaviour; Stress corrosion cracking; Microstructural analysis

1. Introduction

Additive manufacturing emerges as a promising production method that yields significant reductions in production time, energy consumption, and cost, especially for components with complex geometries [1]. Among various additive manufacturing techniques, laser powder bed fusion (L-PBF) has exhibited its superiority in producing components with mechanical properties comparable to or surpassing those achieved through conventional methods [2]. The application of L-PBF for processing Ni-Fe-Cr-based alloy 718 has gained substantial interest in recent years, particularly in industries such as oil and gas, energy, and nuclear sectors [3,4]. This heightened interest can be attributed to the

alloy's capability to offer a compelling combination of exceptional mechanical properties and corrosion resistance, meeting the strict requirements of such industries.

Alloy 718 is well-regarded for its outstanding mechanical properties, primarily owing to the presence of precipitation-hardening secondary phases, namely γ' (Ni3(Al, Ti)) and γ" (Ni3Nb) [5]. However, undesirable phases, including M23C6, M6C, MC carbides, and platelike and blocky δ-Ni3Nb phases at grain boundaries, inevitably form during solidification and aging heat treatments [6–9]. The existence of these unwanted phases is known to significantly reduce the corrosion and stress corrosion cracking resistance (SCC) of conventional alloys under demanding working conditions [10–13]. Research conducted by multiple groups has indicated that the formation of chromium-based carbides may contribute to decreased corrosion resistance through mechanisms such as reduced availability of chromium for passive layer formation, localized corrosion sites adjacent to these phases (sensitization), and the creation of electrochemically coupled environments [14–18]. Consequently, the reduction of carbon content in the alloy is a common strategy to mitigate carbide formation in conventionally produced alloys. However, during the L-PBF process, the formation of such phases is substantially inhibited due to the extremely rapid cooling of the melt pools [19–21]. Instead, the formation of non-equilibrium phases enriched in specific alloying elements (such as Nb and Mo, reaching 2–5 times higher levels for L-PBF compared to conventional alloy 718) at subgrain boundaries in additive manufactured materials has been extensively reported [22–24]. Therefore, a critical question that arises is whether the reduction of carbon content in the metal feedstock used for L-PBF process could impact the corrosion and SCC resistance of the material under the extreme solidification conditions inherent to the L-PBF process. The nominal carbon content of this alloy (for both bulk and powder for L-PBF processing) adheres to standard specifications, with a maximum limit of 0.08 wt.%.

Existing literature on the corrosion performance of additively manufactured alloy 718 has predominantly focused on comparing LPBF with traditional materials and assessing the impact of various heat treatment regimens on corrosion and SCC susceptibility[25]. In general, the outcomes are varied and in some cases contradictory. Luo et al. [26] observed the formation of fine γ', γ", and δ phases after heat treatment, along with the dissolution of enriched subgrain boundaries, resulting in enhanced corrosion resistance. In contrast, Zhang et al. [27] reported superior corrosion performance of as-received L-PBF 718 in comparison to the solution heat-treated case, attributing it to the presence of compressive residual stresses and the absence of δ phases in the as-printed state. In a separate study, Du et al. [28] emphasized an enhancement in corrosion resistance with an increased laves phase density achieved by altering the build orientation. This improvement was explained in terms of an increase in the incline angle, coupled with changes in grain boundary structure and density. Furthermore, in authors prior investigations [29,30] on L-PBF processed alloy 718, the mechanism of SCC initiation, which involves the formation of a coupled environment between the cellular matrix

and subgrain boundaries enriched in Nb and Mo, was elucidated implementing novel microcapillary electrochemical techniques. This leads to selective dissolution of the cellular matrix, combined with the presence of a high dislocation density adjacent to cell boundaries, resulting in a higher energy level at such sites and rendering them more susceptible to both mechanical rupture and corrosion occurrences.

While extensive research has explored the impact of carbon content on the corrosion resistance of alloys with a native oxide layer, a comprehensive understanding of the passive layer characteristics and corrosion behaviour in additively manufactured materials in response to minor variation of carbon content remains lacking. Generally, the reduction in carbon content results in diminished availability of carbon for carbide formation and a significant sensitization adjacent to secondary carbide phases [31].

Moreover, limited investigations into the influence of carbon content in additively manufactured cases by Zhou et al. [32], and Zheng et al. [33] have primarily focused on elucidating the microstructural and mechanical alterations resulting from variations in carbon content within additive manufacturing techniques. These studies suggest that increase in carbon content could be associated with improved mechanical properties as a consequence of dislocation pinning during the movement of dislocations under tensile loading. However, no link has been made between minor variations in carbon content and the corrosion performance of additively manufactured materials. Thus, the current investigation aims to address a critical question: Does reducing carbon content in additively manufactured materials enhance corrosion performance, even though lower carbon content does not contribute to carbide reduction (as a consequence of rapid solidification processes involved)? If so, what mechanism underpins this improved corrosion performance?

This study is dedicated to investigating the behaviour of passive layer and its correlation with submicron structure of two variants of L-PBF processed Alloy 718, which differ in their carbon content. Electrochemical techniques were applied in a chloride-containing solution for evaluation of the corrosion resistance of the specimens and asses the passive layer characteristics. The selection of such environment is based on its relevance, as chloride contamination is a prevalent issue in critical industries, including oil and gas, as well as nuclear power plants situated in coastal regions. The electrochemical investigations were complemented with Scanning Electron Microscopy (SEM), Scanning Kelvin Probe Force Microscopy (SKPFM), X-ray Diffraction (XRD), X-Ray Photoelectron Spectroscopy (XPS), Electron Back Scattered Diffraction (EBSD), and High-resolution Transmission Electron Microscopy (TEM) characterization equipped with Energy Dispersive Spectroscopy (EDS), to analyse in detail the microstructure of the specimens and the characteristics/composition of their surfaces/passive oxide layer.

2. Materials and methods

The selection of carbon content levels for this study is justified in the specifications of existing standard 718 alloys. Traditionally, there are two variants of alloy 718: the conventional aerospace variant and the corrosion-resistant variant (AMS-ASTM F3055–14a, and CTP-ISO-NiCr19Nb5Mo3). While reducing carbon content in conventional materials is beneficial for minimizing carbide formation, this rationale does not apply to additive manufacturing materials due to the rapid solidification processes involved, which lead to the formation of non-equilibrium phases. Additionally, investigating higher carbon content is impractical due to the standard limitations for alloy 718, as any carbon content beyond the standard range would not be relevant.

2.1. LPBF sample preparation

Gas atomized powder of Alloy 718 was employed, specifically utilizing two variants: alloy 718CTP (ISO-NiCr19Nb5Mo3) with lower carbon content (0.045 wt.%), and the standard variant (UNS-N07718, identified by ASTM F3055–14a), containing 0.08 wt.% carbon, provided by VDM metals GmbH, Germany. The particle size range of the powder was 10 µm to 55 µm. Parts fabricated using the low-carbon-content powder are going to be referred to in the text as 718CTP, and samples fabricated with the standard carbon content as 718AMS. The nominal composition of the powder used for the L-PBF process is reported in Table 1. Specimens measuring 30×10×30 mm were processed using an EOS M100 laser metal fusion machine equipped with a 200 W fibre laser. Preliminary experiments were conducted to determine the optimal process parameters for achieving specimens with maximum density. The selection of the most favourable combination of process parameters, including layer thickness of 20 µm, hatch spacing of 70 µm, laser power of 115 W, and a bidirectional alternating chess scan strategy, along with a laser spot diameter of 30 µm, resulted in the highest density in the current investigation.

Considering that evaporation of certain elements can occur during the L-PBF process, the elemental composition of the specimens after printing was measured by EDS-SEM. The EDS analysis revealed minimal compositional variation in nickel, chromium, and molybdenum content for the samples, as summarised in Table 2.

Samples were prepared from the additively manufactured specimens in as-built state through electro-discharge machining (EDM) with dimensions of 10×30×0.8 mm, sliced perpendicular to the build direction. To isolate the influence of the inherent microstructure from potential boundary effects (such as layers attached to the build platform and the final build layer), the first and last 0.5 mm thickness along the build direction were excluded from the analysis. To focus solely on the microstructural impact of the L-PBF process and minimize the influence of the EDM process on surface morphology, specimens were precisely ground and polished up to 0.1 µm alumina suspension. Subsequently, the samples underwent a 15-minute ultrasonic wash in a 30% ethanol solution, followed by rinsing with

pure ethanol. The specimens were left undisturbed for 72 hours to allow for the formation of a native oxide layer on the surface under identical environmental condition.

Table 1. Nominal composition of the powder used for L-PBF manufacturing. 718AMS refers to the standard alloy, while 718CTP refers to the low carbon content variant.

Sample/wt. %	Ni	Cr	C	Mn	Si	Cu	Mo	Nb	Al	Ti	Fe
718CTP	50-55	17-21	0.045	0.35	0.35	0.23	2.8-3.3	4.85-5.2	0.40-0.6	0.80-1.15	Bal.
718AMS	50-55	17-21	0.08	0.35	0.35	0.3	2.8-3.3	4.75-5.5	0.20-0.8	0.65-1.15	

Table 2. EDS elemental compositional analysis of L-PBF Processed specimens. 718AMS refers to the standard alloy, while 718CTP refers to the low carbon content variant.

Sample/wt. %	Ni	Cr	Fe	Mn	Si	Cu	Mo	Nb	Al	Ti	C
L-PBF 718 CTP	51.2	18.7	17.38	0.4	0.2	0.2	4.4	6.1	0.7	0.7	0.02
L-PBF 718 AMS	51.3	18.8	17.4	0.3	0.3	0.2	4.2	6	0.6	0.84	0.06

2.2. Micro and submicron characterization

A thorough microstructural analysis was conducted on the specimens both before and after undergoing electrochemical polarization experiments. Pore analysis was performed using a Leica DMRE optical microscope, capturing images at magnifications of 5X, 10X, and 20X, with a total of 30 images obtained for all magnification levels. For microstructural analysis of the as-built specimens, etching with Kalling's 2 reagent (2 g CuCl2, 40 ml HCl, 8 ml Ethanol) was employed. Subsequently, subgrain width analysis was performed on the etched surfaces analysed by SEM and TEM. Notably, the analysis encompassed 20 SEM pictures at a magnification of 10,000X, taken from different zones on the surface of the specimens (perpendicular to the build direction, where the electrochemical polarization experiments were conducted), in conjunction with 30 images derived from TEM analysis of successive samples, with an electron energy of 15 KeV. To ensure statistical significance, a total of 1,500 subgrain measurements were conducted. To characterize the microstructure of the as-built specimens, FEI QUANTA 250 field emission SEM (FE-SEM) equipped with Oxford instruments EDS detector was utilized.

TEM analysis was conducted using a JEOL JEM-F200 instrument equipped with EDS detector, operating at an acceleration voltage of 200 kV. TEM samples were prepared by hand grinding until a

thickness of up to 40 µm was achieved. Subsequently, electrochemical polishing was carried out using the STRUERS TENUPOL-3 twin-jet polishing unit, utilizing a solution consisting of 95% acetic acid and 5% perchloric acid until reaching electron transparency. The electrochemical polishing was performed at 45 V and at a temperature of -25 degrees Celsius.

2.3. X-ray Diffraction

XRD measurements were conducted for the identification and quantification of phases. The measurements utilized a Siemens D500 X-ray diffractometer (Siemens, Munich, Germany) equipped with a Cu Kα radiation tube, operating at 40 kV and 30 mA. The analysis covered a 2θ angular range from 40 to 105°, with a scan step of 0.025° and a counting time of 3 s per step.

2.4. Electron back scattered diffraction analysis

EBSD analysis was performed using a FEI QUANTA 250 FEG-SEM equipped with an AMETEK EBSD Detector. Specimens were polished with a final polishing step using 40 nm colloidal silica. The SEM was operated at an accelerating voltage of 20 kV. EBSD data was collected across a representative area of 400 µm ×400 µm surface with a step size of 1 µm to ensure adequate spatial resolution. Kernel Average Misorientation (KAM) maps were generated from the EBSD data to quantify local lattice distortion and dislocation density. To enhance data reliability, EBSD and KAM analyses were conducted at three distinct locations on each sample. The acquired EBSD data was processed using OIM Analysis software to generate inverse pole figure (IPF) and KAM maps of the surface. Statistical analysis of KAM values and grain size distributions was performed to evaluate microstructural variations between different samples.

2.5. Scanning kelvin probe force microscopy

SKPFM was implemented using a Park Systems XE–100 atomic force microscope. The measurements utilized rectangular conductive cantilevers (ANSCM–PT from AppNano) coated with Pt/Ir, exhibiting a nominal resonant frequency ranging from 50 to 70 kHz and a nominal spring constant between 1 and 5 N/m. A dynamic mode with a single-pass approach was employed for analysis, allowing the simultaneous acquisition of topography and corresponding potential images. The acquired potential signal, referred to as the contact potential difference (CPD) between the tip and the sample, reflected the discrepancy in the work function of the probe and the surface. To accurately depict the relationship between the Volta-potential values of the investigated surface, the recorded potential signal was inverted.

SKPFM measurements were sequentially conducted on specimens, and upon completing the analysis of the last specimen, the initial sample was re-measured. This step ensured that the volta potential of the probe remained unchanged, ruling out any effects from wear, geometrical alterations of the tip apex, or contamination [34]. The consistent CPD value obtained in the second scan of the initial

sample confirmed the stability of the AFM probe and facilitated the direct comparison of CPD values across different specimens. These CPD values represent the Volta potential difference between the surface of each sample and the probe. With no variation in the Volta potential of the probe, discrepancies between the measured CPD values indicate variations in the Volta potential of the analysed specimens.

2.6. X-ray Photoelectron Spectroscopy

XPS experiments were conducted using an EnviroESCA spectrometer (Specs) equipped with an AlKα X-ray source (hυ = 1486.6 eV). The analyses took place under vacuum conditions, maintained at approximately 10^{-6} mbar. High-resolution spectra were acquired with a pass energy setting of 30 eV, integrating for 0.2 seconds per step and recording data at 0.1 eV intervals per step. To mitigate experimental discrepancies caused by charge accumulation, an adjustment in binding energy (BE) was applied. Specifically, a BE correction of 284.8 eV was used to account for the presence of adventitious carbon [35]. Further analysis included the decomposition of XPS spectra using Keystone software (Specs) with a Shirley-type background subtraction [36]. Quantification parameters for the analysis were provided by Specs.

2.7. Electrochemical polarization analysis

The microcapillary test method was employed to carry out electrochemical polarization experiments, offering a viable alternative to conventional techniques for investigating corrosion at the microscale. The implementation of this method facilitates the early-stage observation and analysis of localized corrosion phenomena, including pitting and SCC, due to its high sensitivity to even subtle changes and its ability to examine small surface areas. Additionally, this method allows for multiple electrochemical experiments to be conducted on the same test surface, minimizing the potential data scattering caused by variations in surface morphology. In all experiments, an open circuit potential (OCP) measurement was conducted for one hour to establish equilibrium between the electrolyte and the specimen. The OCP values, relative to the standard calomel electrode (SCE), were determined to be -200 ± 10 mV for low-carbon and -210 ± 10 mV for high-carbon specimens. The three-electrode configuration with calomel electrode as reference and platinum wire as the counter electrode was utilized. A Gamry Interface 1010E potentiostat unit from Gamry Instruments (USA) was utilized for the electrochemical measurements.

Electrochemical impedance spectroscopy (EIS) was carried out on a circular area with a 3 mm diameter, covered with strong adhesive tape. The frequency range was set between 0.01 and 10^{-5} Hz, with a DC amplitude based on OCP with respect to SCE values for each specimen and an AC amplitude of 10 mV.

Potentiodynamic, Mott-Schottky, galvanostatic (constant current density) and potentiostatic (constant potential) polarization experiments were performed using the microcapillary technique to comprehensively understand the alterations in electrochemical behaviour among the specimens. A solution of 3.5% sodium chloride in deionized and deaerated water (bubbled with pure argon for 20 minutes before experiments) was employed to replicate common chloride ion contamination found in critical industries, especially those located in coastal regions. The contact surface was circular with a diameter of 500 μm, and the microcapillary tip was sealed with silicon glue to prevent crevice corrosion at the interface. Due to the self-isolation nature of the microcapillary method, the solution remained isolated from the environment, eliminating environmental factors from affecting the measured data.

Potentiodynamic polarization measurements were performed in the range of -0.5 to 1.5 V with respect to OCP, measured prior to the experiments, at a scan rate of 1 mV/s. Mott-Schottky polarization measurements were conducted after polarizing the samples for one hour at a potential corresponding to the passive region (200 mV vs. SCE for both specimens obtained from potentiodynamic polarization results) to ensure a uniform passive layer on the surface of both specimens. The potential range of -0.5 to 1 V, a scan rate of -50 $mV.s^{-1}$, and an AC amplitude of 10 mV at 1 kHz were used to examine the effect of carbon content variation on the semiconductor behaviour of the materials.

To understand the behaviour of the native oxide layer under tensile loading conditions, for further characterization of SCC crack initiation, specimens were tensile strained at 0.2% strain corresponding to the yield stress of the material (0.2% proof stress). To ensure experimental reproducibility, identical specimens were employed for both polarization experiments and subsequent analyses. Measurements were consistently conducted at the specimen centre, with each experimental condition replicated at least on two specimens. Tensile straining was accurately measured using a DT9829 high-precision mixed sensor USB device (Measurement Computing Corporation, USA) combined with strain gauges in half Wheatstone bridge configuration. Galvanostatic measurements were conducted with a constant current density maintained at a level proximate to the breakdown current density determined from potentiodynamic polarization measurements, lasting for a duration of 3000 seconds. Additionally, potentiostatic measurements were carried out by maintaining a constant potential, set at a value 10% lower than the breakdown potential obtained from potentiodynamic polarization measurements, for each specimen.

3. Results

3.1. Microstructural analysis and phase characterization

Analysis of specimen density using the Archimedes method revealed a density of 99.89% for the AMS alloy and 99.91% for the CTP alloy, indicating the production of nearly fully dense specimens for both conditions. Additionally, optical microscope examination of the pore surface area obtained

from cross sectioning the specimens (depicted in Figure 1a) further confirmed the high density of both alloys. The observed pores are predominantly spherical, indicative of gas entrapment during the L-PBF process.

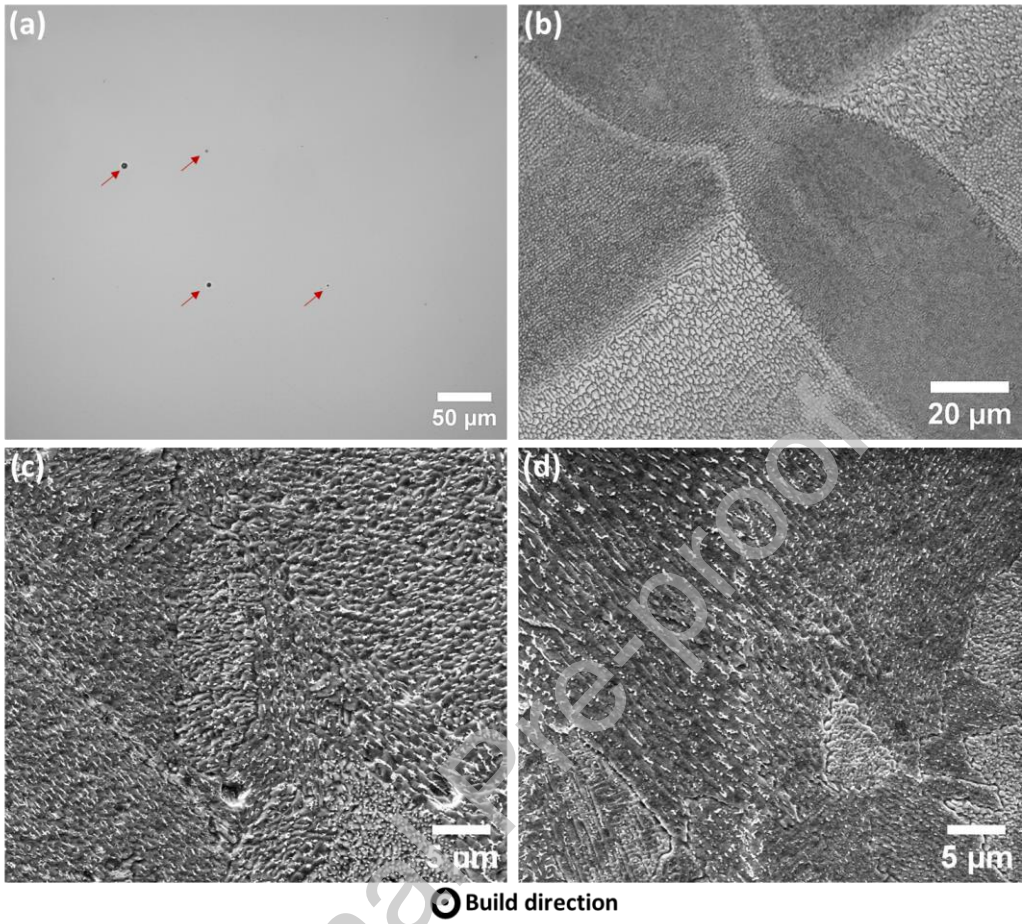

Figure 1. (a) Optical images of the surface indicating overall pore shape (shown by red arrows), (b) SEM image at low magnification for CTP specimen, (c) higher magnification images for CTP, and (d) for AMS alloy.

SEM analysis of the etched surface for both alloys, as illustrated in Figure 1b-d, highlights an identical microstructure characterized by a submicron cellular-columnar structure separated by non-equilibrium precipitates at cell boundaries. This specific microstructure and the presence of both columnar and cellular structure is frequently observed in as-built structure for L-PBF processed austenitic stainless steels and nickel-based superalloys [28,37–39]. It is well-documented that the cell boundaries within this microstructure are enriched in certain alloying elements, such as molybdenum and niobium, in the case of alloy 718 [22–24].

To analyse the influence of variations in carbon content on cell size, a statistical analysis of the cell size was conducted on both TEM and SEM images. The statistical analysis of the cell size, as illustrated in Figure 2, reveals nearly identical cell sizes for both cases. This suggests a higher impact of process parameters (which remain consistent for both alloys) on cell size compared to minor

variations in chemical composition. It is noteworthy that the solidification rate in L-PBF processed materials is widely recognized to be influenced by process parameters such as laser power, scan speed, layer thickness, etc [1,2].

Additional XRD analysis, as illustrated in Figure 3, was conducted on the specimens in the longitudinal direction. The results revealed a nearly identical XRD pattern for both alloys, indicating that the carbon content has no significant impact on the XRD patterns.

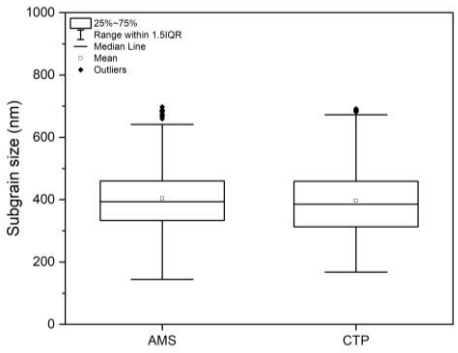

Figure 2. Subgrain size comparison for the CTP and AMS specimens.

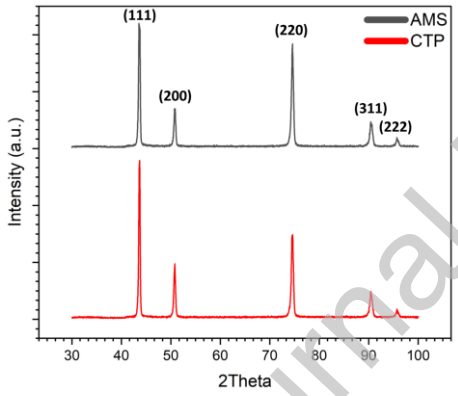

Figure 3. XRD pattern comparison for both high carbon AMS and low carbon CTP alloys.

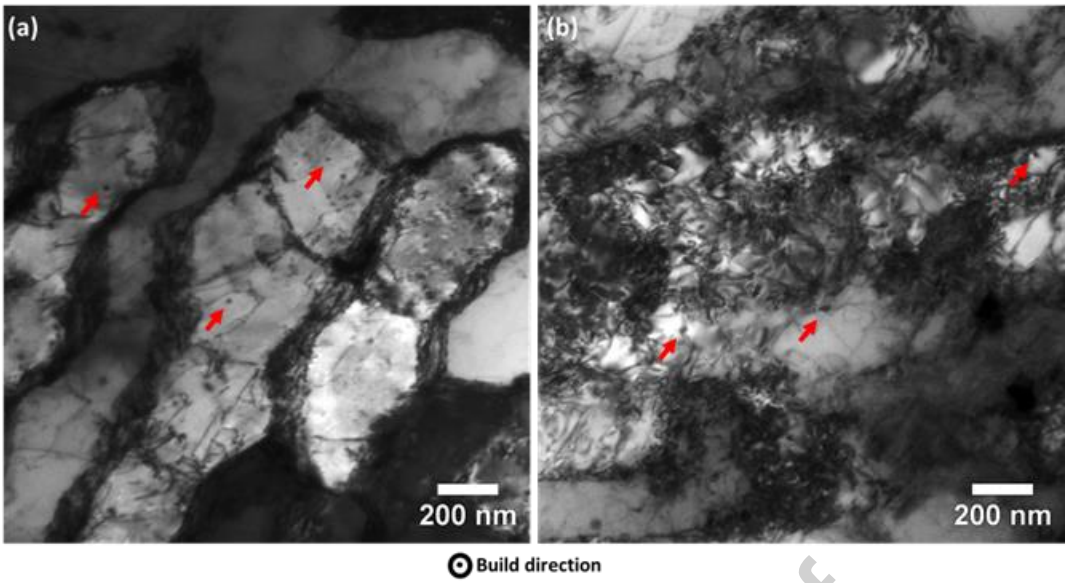

Figure 4. TEM analysis of (a) low carbon 718CTP alloy, and (b) higher carbon 718AMS specimens. Presence of secondary phases (shown by red arrows).

To delve more deeply into the effects caused by variations in carbon content, TEM analysis was conducted. It is important to note that TEM analysis was carried out on five specimens prepared from different areas on the sample. For each TEM specimen, 30 images were analysed to ensure the reliability of the reported pictures. TEM analysis of the specimens, as depicted in Figure 4, reveals a significant increase in dislocation density for the alloy with higher carbon content. However, the presence of secondary phases (shown in Figure 4) was nearly identical for both alloys, and no conclusive remarks regarding the effect of carbon content on the formation of precipitates could be drawn.

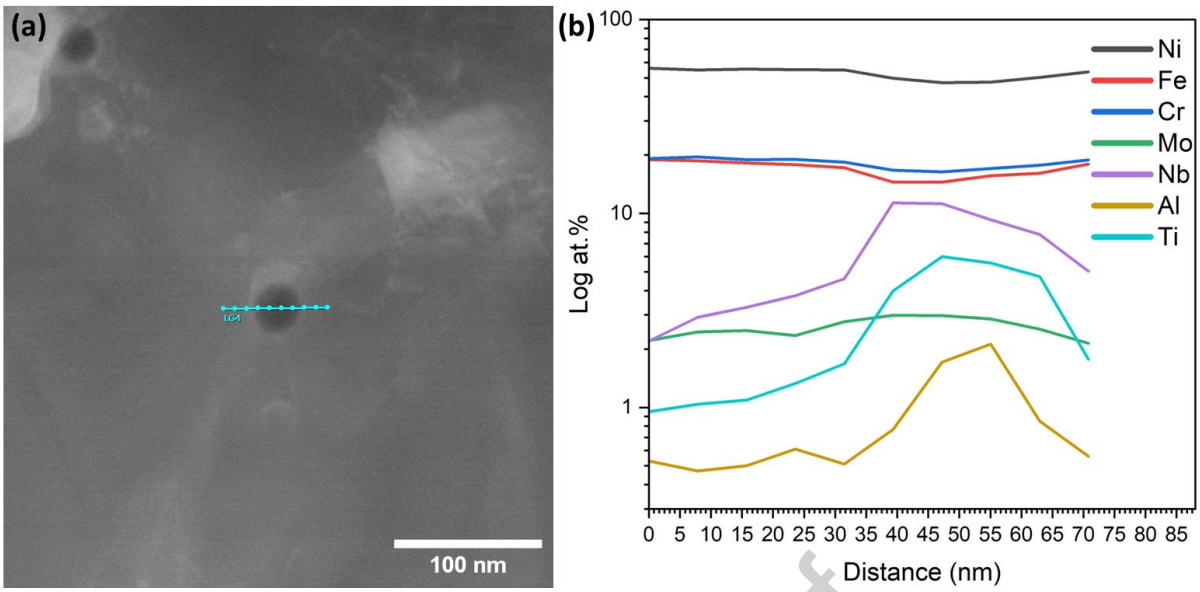

Figure 5. Line scan TEM-EDS analysis of submicron particles for the CTP alloy (due to similarities in the shape and EDS results, the line scan and image of AMS alloy is not shown herein).

Further line scan analysis of the particles highlighted the dominant presence of γ'-Ni3(Al,Ti), and γ''-Ni_3Nb with a dimension of less than 30 nm (see Figure 5). However, statistically analysing the TEM data from various sites and magnifications (from 30 TEM images), it was predominantly observed that specimens with higher carbon content exhibited a greater dislocation density.

3.2. EBSD analysis

IPF maps provided information on crystallographic orientation distribution, revealing the texture of the material, while KAM maps quantified local lattice distortion, indicative of dislocation density and strain. Figure 6 presents EBSD- IPF maps depicting the Face-Centred Cubic (FCC) austenite phase and the corresponding KAM maps of the specimens. The KAM results are summarised in Table 3.

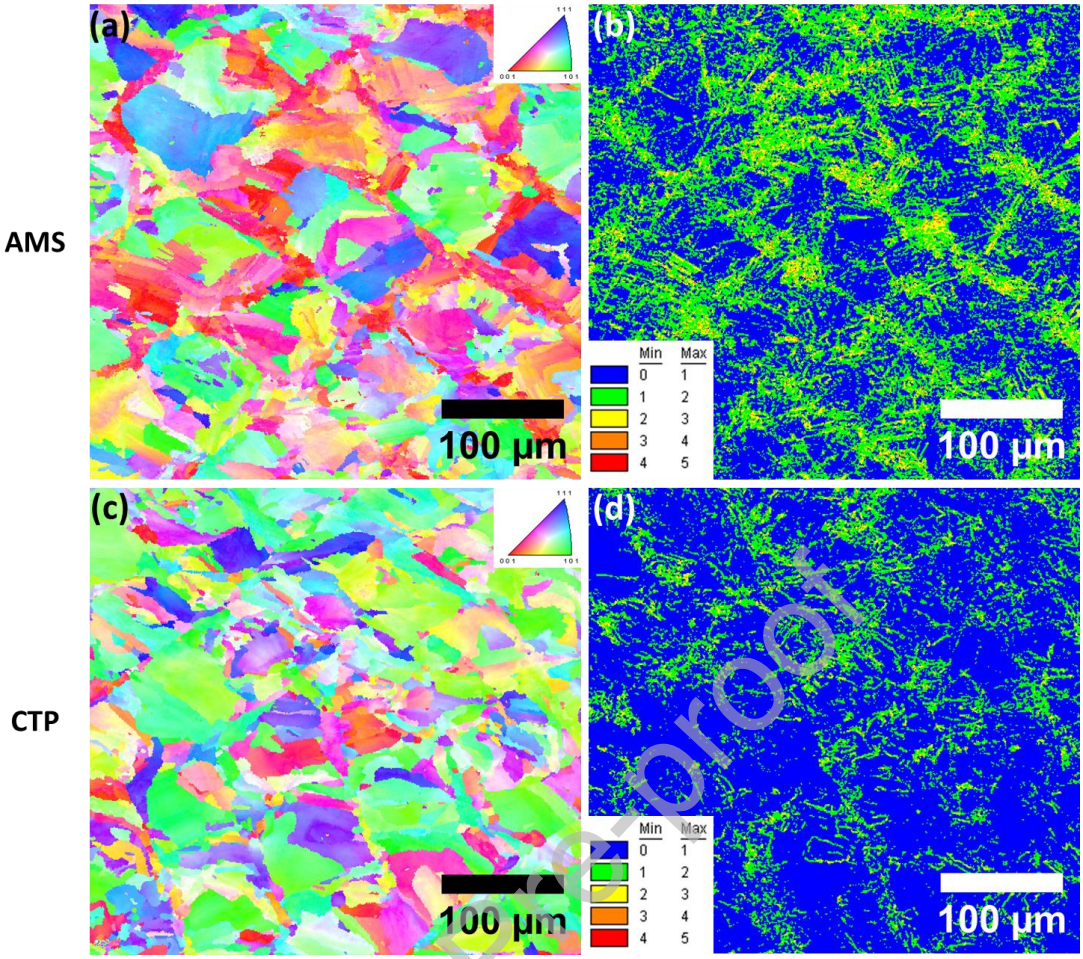

Figure 6. EBSD inverse pole figure (IPF) maps and kernel average misorientation (KAM) maps of (a), (b) L-PBF processed alloy 718 AMS, and (c), (d) CTP alloy.

KAM maps offer insight into the distribution and magnitude of local strain within the microstructure. The KAM value is a measure of the local misorientation angle, which correlates with the density of geometrically necessary dislocations (GNDs). These dislocations accommodate plastic deformation gradients, reflecting the material's local mechanical response to stress. The IPF maps demonstrate a consistent crystallographic orientation across the specimens. Analysis of the KAM maps reveals that the high-carbon material exhibits significantly higher average KAM values compared to the low-carbon CTP samples. It is important to note that EBSD and KAM analyses were conducted at three distinct sites of equal size on the surface, and the standard deviation after multiple analyses was less than 0.5%. The observed higher average KAM values in high-carbon material indicated a greater density of GNDs, suggesting that these materials experience higher internal strain energy.

Table 3. Kernel average misorientation for the L-PBF processed alloy 718.

Angle (degree)		0-1	1-2	2-3	3-4	4-5
Total Fraction	AMS	0.679	0.364	0.063	0.010	0.001
	CTP	0.562	0.278	0.038	0.005	0.001

3.3. SKPFM analysis

Figure 7a and b, show representative examples of topography and Volta potential maps of the AMS specimen's surface. Considering the scale of the topographic image, the observed scratches on the surface (from the sample polishing) were only less than 3 nm in depth and had no influence on the surface activity of the material. Owing to similarities with the AMS data, the corresponding information for the CTP specimen is omitted. The Volta potential maps generated via SKPFM (Figure 7b) illustrate the surface potential in relation to the metal probe, known as the CPD. The measured CPD values obtained through SKPFM directly reflect the specimen's work function, providing valuable insights into its surface condition [40]. In instances where a metal or alloy is coated with a thin native oxide layer, the work function closely correlates with the properties of this oxide film, such as thickness and passivity, leading to higher CPD values with thicker or more resistive/noble oxide layers.

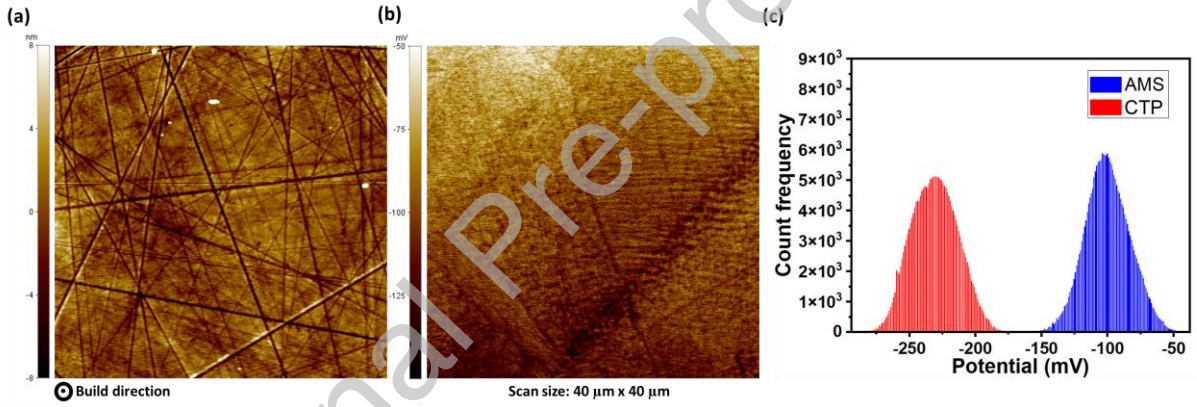

Figure 7. SKPFM analysis of the specimens (a) topography, (b) Volta potential map, and (c) comparison and distribution of CPD values.

The surface potential distribution of the specimens, as depicted in Figure 7c, showcases a relatively uniform pattern. This uniformity is attributed to the microstructural refinement achieved through the rapid solidification process inherent in the manufacturing technique. To explore the impact of carbon content on the surface CPD condition, a statistical analysis was performed on the data collected from various regions and resolutions. As shown in Figure 7c, specimens with higher carbon content consistently exhibited elevated CPD values compared to those with lower carbon content. Additionally, the symmetrical shape of the potential distribution (Figure 7c) across both cases confirms a relatively uniform microstructure at the microscale, irrespective of carbon content. Notably, the calculated nanoscale surface roughness (R_a) derived from Atomic Force Microscopy images ranged from 1 to 1.7 nm, indicating minimal roughness. Thus, it is confidently concluded that the SKPFM results were predominantly influenced by underlying microstructural features rather than variations in surface roughness.

3.4. XPS Analysis

XPS studies revealed the presence of several elements on the surface of the investigated materials as shown in the survey XPS analysis of Figure 8, consisting of C, O, N, Fe, Ni, Cr, Ti, Nb and Mo. The carbon and oxygen surface concentrations are the highest among the different elements. The quantitative analysis is summarized in Table 4. In order to avoid the contribution of contaminants (e.g., adventitious carbon and adsorbed/chemisorbed oxygen species), the surface metals relative composition obtained from XPS studies is calculated and results are summarized in Table 5. The metal content on the surface of AMS raises in the order Ni > Cr > Fe > Nb > Mo > Ti, while for CTP is Ni > Cr > Nb > Mo > Fe > Ti. When comparing the two samples, it is observed that the surface composition of AMS exhibits relatively higher concentrations of Fe (8.70 vs. 5.81 at.%), Ni (54.23 vs. 53.82 at.%), and Nb (7.47 vs. 6.97 at.%), slightly lower levels of Cr (22.15 vs. 25.72 at.%), and similar levels of Ti (1.09 vs. 1.27 at.%), and Mo (6.36 vs. 6.41 at.%).

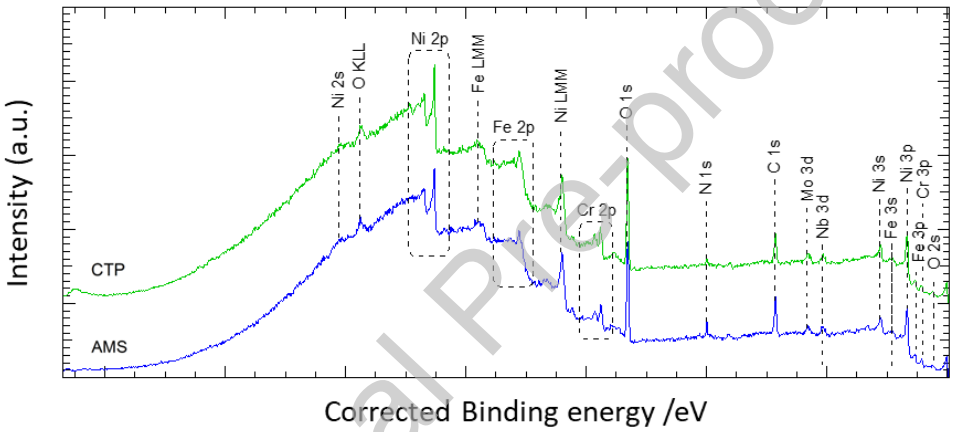

Figure 8. Survey XPS spectra and qualitative analysis of the surface elemental composition of the different samples.

Table 4. Surface elemental composition obtained from XPS studies.

Sample/ at. %	C	O	Fe	Ni	Cr	Ti	Nb	Mo	N
AMS	39.06	39.87	1.35	8.43	3.44	0.17	1.16	0.99	5.52
CTP	32.06	44.38	1.1	10.2	4.87	0.24	1.32	1.21	4.61

High-resolution XPS investigations reveal the presence of four different carbon species (Figure 9a): (i) a minor component of carbides peaking at ca. 282.6 eV; (ii) adventitious sp3 carbon at 284.8 eV; (iii) C-O species at ca. 286.2 eV; and (iv) chemisorbed carbonates cantered at ca. 288.2 eV [41–44]. Three distinct features are observed in the O 1s spectral region of all the samples (Figure 9b). In particular: (i) at low binding energies (BEs), ca. 529.7 eV, the peak is associated to lattice oxygen atoms in the metal oxides framework; (ii) at medium BEs, ca. 531.2 eV, the surface-chemisorbed hydroxyls/carbonates and/or surface metal oxides defects are recognized; and (iii) at high BEs, ca.

532.9 eV, the observed peak is attributed to adsorbed or chemisorbed oxygen species, such as O2 or H2O [45–47].

Table 5. Surface metals relative composition obtained from XPS studies.

Sample/ at. %	Fe	Ni	Cr	Ti	Nb	Mo
AMS	8.7	54.23	22.15	1.09	7.47	6.36
CTP	5.81	53.82	25.72	1.27	6.97	6.41

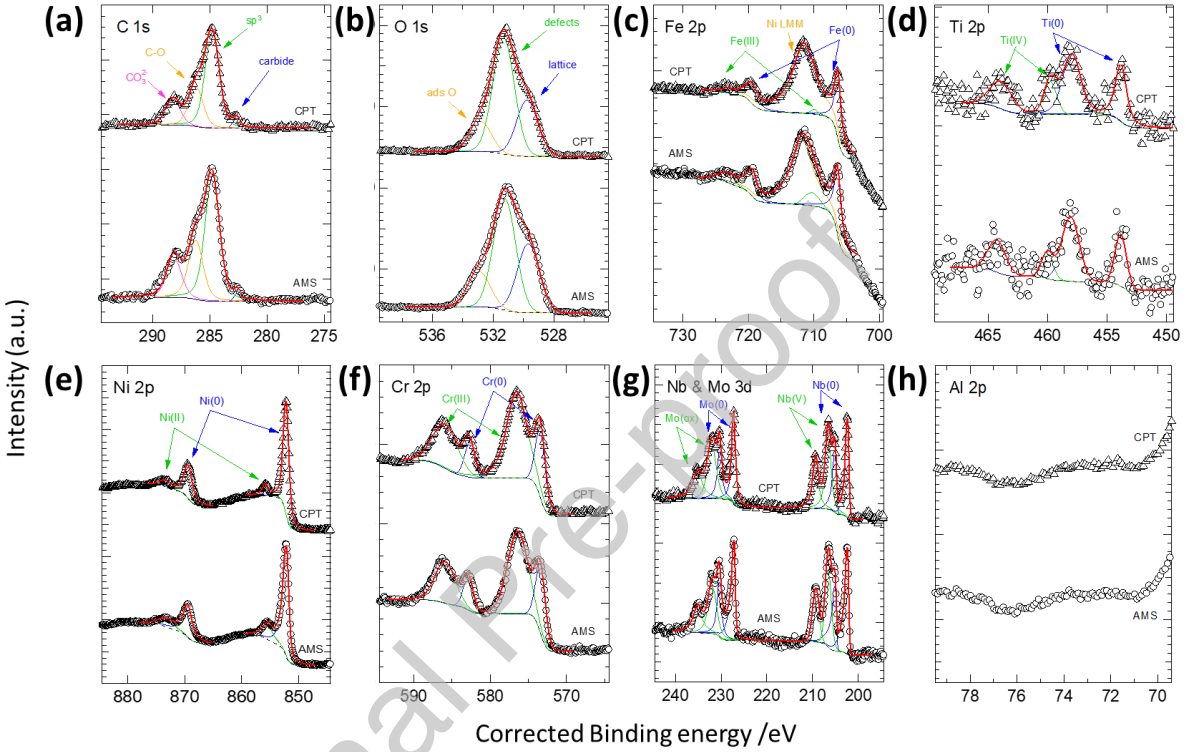

Figure 9. High resolution XPS analysis and fitting of (a) C 1s, (b) O 1s, (c) Fe 2p, (d) Ti 2p, (e) Ni 2p, (f) Cr 2p, (g) Nb and Mo 3d, and (h) Al 2p. Y-axes of the graphs represent Intensity (a.u.)

As expected, in each metal 2p spectral region, peaks are present as couples, resulting from the spin-orbit splitting phenomenon which gives rise to the formation of the 2p3/2 (low BEs) and 2p1/2 (high BEs) features. Similarly, in the metals 3d spectral region, peaks are separated in their 3d5/2 (low BEs) and 3d3/2 (high BEs) features. In the Fe 2p spectral region (Figure 9c), two different iron species are detected, with the 2p3/2 peaking at ca. 706.3 and 710.2 eV, respectively. The former is assigned to iron in the metallic state, and the latter to Fe(III) species [48,49]. The Ni LMM line is also present in this spectral range. In both samples, iron is mainly present as Fe(0), however, more oxidized iron was detected in AMS sample compared to CTP specimen (Table 6). The presence of two different nickel species is observed in the Ni 2p spectral region (Figure 9e): (i) Ni(0) peaking at ca. 852.2 eV; and (ii) Ni(II) in the form of hydroxides centred at ca. 855.6 eV [50,51]. Similarly to Fe, also Ni surface atoms are mainly present in their metallic form, with AMS more oxidized with respect to CTP (see Table 6).

Table 6. Relative intensities (in %) of the different oxidation states of surface metals atoms obtained from XPS studies.

Sample	Fe		Ni		Cr		Ti		Nb		Mo	
	Fe(0)	Fe(III)	Ni(0)	Ni(II)	Cr(0)	Cr(III)	Ti(0)	Ti(IV)	Nb(0)	Nb(V)	Mo(0)	Mo(ox)
AMS	76.34 ±1.44	23.66 ±1.44	79.00 ±0.86	21.00 ±0.86	26.11± 1.57	73.89 ±1.57	34.21 ±2.76	65.79 ±2.76	52.24 ±1.97	47.76 ±1.97	51.23 ±1.32	48.77± 1.32
CTP	92.15 ±2.20	7.85± 2.20	87.30 ±0.68	12.70 ±0.68	23.01 ±0.70	76.99 ±0.70	40.38 ±2.59	59.62 ±2.59	42.25 ±1.38	57.75 ±1.38	46.92 ±1.22	53.08± 1.22

The Cr 2p spectral region (Figure 9g) reveals the presence of two Cr species: (i) at ca. 573.4 eV, Cr(0) species were detected; and (ii) at ca. 576.4 eV, surface chromium is present as Cr2O3 [52,53]. In the case of chromium, the oxidized species are mainly present (see Table 6), with a similar content between the two compositions. In the Ti 2p spectral region (Figure 9d), two different titanium species were detected, with the 2p3/2 peaking at ca. 453.8 and 458.0 eV, respectively. The former is assigned to titanium atoms in their metallic state, and the latter to Ti(IV) species. Titanium species are mainly present as TiO2 (see Table 6), and the slightly more oxidized character of the AMS sample is confirmed also for this element. The presence of two different niobium species is observed in the Nb 3d spectral region (Figure 9g): (i) Nb(0) peaking at ca. 202.4 eV; and (ii) Nb(V) centred at ca. 206.6 eV. The surface concentration of metallic and oxidized niobium species is almost the same (see Table 6), with the AMS sample exhibiting slightly less oxidized Nb. Finally, molybdenum species are detected as (Figure 9g): (i) Mo(0) at ca. 227.2 eV; and (ii) oxidized Mo species (i.e., IV, V or VI) at ca. 231.9 eV. Mo shows a similar behaviour with respect to Nb, with similar ratio between the metallic and oxidized forms. No surface aluminium species are detected in the samples (Figure 9h).

In general, while the overall peak shapes and positions for various elements (specifically for Fe, Cr, and Ni) in the high-resolution XPS spectra (Figure 9) suggest the presence of identical oxide/hydroxide species on the surfaces of both alloys, the key difference lies in the relative intensities of these oxide peaks compared to the signal from the underlying metallic elements, indicating variations in surface oxide layer thickness. It is essential to emphasize that while alloy 718 comprises several elements, nickel, iron, and chromium are the primary constituents influencing its corrosion behaviour. High-resolution XPS analysis revealed a substantial difference in oxide state intensities between nickel and iron, sufficiently large to be considered statistically significant, even when accounting for experimental error (standard deviation of 1% after repeating the survey XPS spectra for 3 times) and fitting uncertainties. This pronounced disparity provides strong evidence supporting the formation of a thicker outer layer enriched in iron and nickel oxides compared to the underlying chromium-rich oxide scale.

The oxide layer thickness can be calculated from XPS results using the following equation [54,55]:

$$d = \lambda_o . \sin(\theta) . \ln[1 + \frac{N_m \lambda_m}{N_o \lambda_o} \frac{I_o}{I_m}] \qquad (1)$$

Where d is the thickness, N_m/N_o the ratio of the volumetric densities of atoms in metal to oxide, λ the inelastic mean free path (IMFP) of the photoelectrons, and I the XPS peak intensity of the element for the metal (m) and oxide (o). Parameters for the calculation of the oxide layer thickness were obtained from NIST Electron Effective-Attenuation-Length Database, [56], and [54] which are summarized in Table 7. It is noteworthy that the presence of nickel, likely in the form of hydroxides, necessitates a slightly different approach for calculating layer thickness which is well established in the literature [54].

Table 7. Parameters used for oxide layer thickness calculation.

Composition	λ(nm)	N(atoms.cm^{-3})
Fe_2O_3	1.926	1.97E+22
Cr_2O_3	1.950	2.07E+22
$Ni(OH)_2$	2.102	2.70E+22
Fe	1.624	8.49E+22
Cr	1.660	8.32E+22
Ni	1.490	9.12E+22

Table 8 summarizes the findings of the thickness of the oxide layers extracted from XPS analysis. Notably, the thickness of the inner chromium-enriched oxide layer exhibits minimal variation between the AMS and CTP specimens. Conversely, the outer iron oxide layer displays a marked difference in thickness. AMS specimens possessed a significantly thicker iron oxide layer compared to their low-carbon CTP counterparts.

The interplay between native oxide layers and the complex interactions of nickel and iron oxides/hydroxides during outer layer formation necessitates caution when interpreting the following calculations and results. These values should be considered estimations based on XPS data and may deviate from the actual thickness due to the inherent limitations of this approach. Furthermore, it is essential to emphasize that Equation 1 provides a relative thickness estimation. While the oxide layer comprises multiple elements, a reasonable approximation of relative thickness can be achieved by focusing on the element with the most significant contribution to oxide formation. However, the key observation derived from the analysis of oxidation states was that the high carbon AMS specimen showed elevated levels of Ni and Fe oxides in the passive oxide layer, whereas the Cr oxides remained relatively consistent across both alloys.

Table 8. Calculated oxide layer thickness for each layer obtained from XPS results.

Composition	Thickness (nm)	
	CTP	AMS
Cr_2O_3	4.92	4.62
Fe_2O_3	0.52	1.45
$Ni(OH)_2$	1.63	3.34

3.5. Electrochemical polarization characterization

In previous investigations conducted by the authors, the microcapillary technique has proven to be a robust method for comprehensive characterization of corrosion properties, particularly stress-assisted corrosion behaviour [29,30,57,58]. This method is instrumental in shedding light on the initiation of surface cracks, a scenario where conventional methods often fall short due to the large surface area in contact with the solution. Consequently, in past decades, less attention has been devoted to understanding the initial stages of passive layer breakdown under tensile loading conditions.

To understand the influence of carbon content on the corrosion behaviour of Alloy 718, potentiodynamic polarization tests were conducted on as-built samples without external strain (Figure 10a). While the corrosion potential exhibited minimal variation, the breakdown potential and, to a lesser extent, the current density displayed notable differences. The low-carbon alloy showed a higher breakdown potential and a slightly lower current density within the passive region. Notably, both alloys exhibited a passive region (current plateau in the anodic branch), indicating the formation of a passive layer on the surface. Additionally, the low-carbon alloy displayed a lower current density throughout the passive and active-passive regions compared to the higher-carbon alloy.

To evaluate the semiconducting behaviour of the native oxide layer. Mott-Schottky analysis was conducted on the specimens (as shown in Figure 10a) within the potential range considered in the current investigation. Both alloys exhibited two linear segments. The segment with a negative slope signifies the existence of p-type semiconducting behaviour, while the segment with a positive slope indicates the presence of n-type semiconducting behaviour within the passive film. The observed p-type semiconducting behaviour has been attributed in previous studies to chromium oxides in the inner layer, while the n-type semiconducting behaviour has been explained as a result of iron and nickel oxides in the outer layer, highlighting a bilayer passive layer forming on the surface of passive materials (Cr oxide enriched adjacent to metal surface and external Ni-Fe oxide/hydroxide enriched outer layer) [59–66].

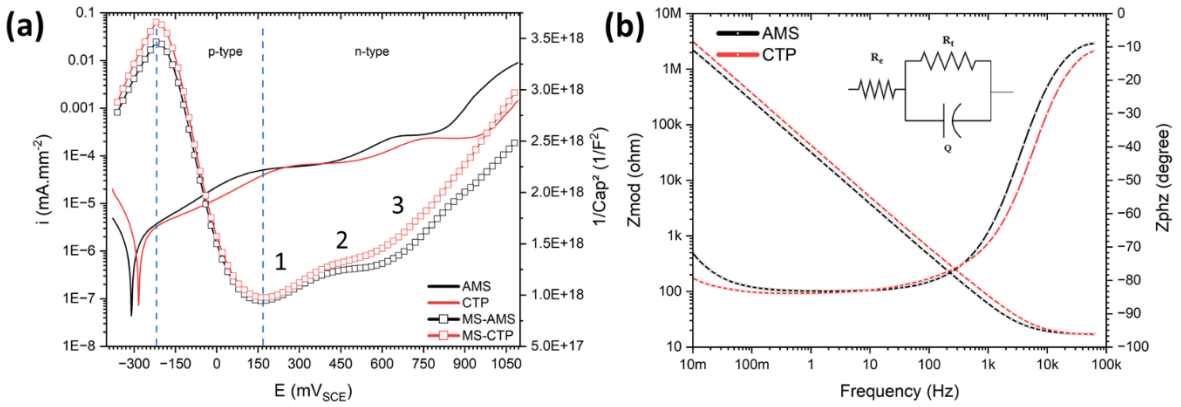

Figure 10. (a) Potentiodynamic polarization curves together with Mott-Schottky analysis of the AMS and CTP alloy 718 obtained in 3.5 wt.% deaerated NaCl solution, and (b) electrochemical impedance spectroscopy (bode and phase angle) curves obtained on the same specimens under the same solution. The inset of the figure represents the equivalent electrical circuit used to model the electrochemical impedance response.

The space charge capacitance for both n-type and p-type semiconductors in both alloys is assessed using the expressions derived from Mott-Schottky theory [67]:

$$\frac{1}{C^2} = \frac{1}{C_{dl}^2} + \frac{1}{C_{SC}^2} + \frac{2}{\varepsilon\varepsilon_0 q N_q}\left(E - E_{fb} - \frac{kT}{e}\right) \qquad (2)$$

The Helmholtz layer capacitance (C_{dl}) and space charge capacitance (C_{SC}) play crucial roles. The donor/acceptor density in the passive film is denoted as N_q, while ε represents the dielectric constant of the oxide (with a specific value of 15.6 for the passive films consisting of chromium oxides [68,69]). Additionally, ε_0 stands for the vacuum permittivity constant (8.85 × 10−14 F.cm^{-1}), e signifies the electron charge (1.602 × 10−19 C), k is the Boltzmann constant (1.38 × 10−23 J.K^{-1}), T denotes the absolute temperature, q is the elementary charge, and E_{fb} represents the flat band potential. In the context of p-type semiconductors, the 1/C versus E relationship exhibits linearity with a negative slope inversely proportional to the acceptor density. Conversely, an n-type semiconductor demonstrates a positive slope inversely proportional to the donor density. The determination of interfacial capacitance C involves the utilization of system software of the potentiostat (Gamry Echem2 Analyst), employing the relation $C=(-Z''2\pi f)^{-1}$, where Z'' denotes the imaginary part of the impedance and f is the frequency.

Mott-Schottky analysis assumes the space-charge layer capacitance dominates at high frequencies (e.g., 1 kHz), rendering Helmholtz layer contributions negligible [70]. The 1. C_{SC}^{-2} vs. E plots then reflect the depletion region's semiconductivity. Charge carrier densities (N_a & N_d) derived from slopes indicate non-stoichiometry, defects, or overall disorder in the passive film [71]. In p-type, acceptor species are cation vacancies, while donor species in n-type films are oxygen vacancies or cation interstitials [71].

As illustrated in Figure 10a, both the acceptor and donor densities exhibit a slight decrease for the low carbon alloy compared to its high carbon counterpart (with the slope inversely related to the density of charge carriers as shown previously). This slight reduction suggests the presence of a more protective native oxide layer on the surface of the low carbon specimens. However, the data presented in Figure 10a suggest a similar trend for both alloys, indicating a comparable chemical composition of the native double-layered oxide on each specimen (n-type, and p-type within identical range). Within this layer, chromium oxide functions as a Schottky barrier, while iron and nickel oxides act as ohmic contacts within the specified potential range. Additionally, a higher density of charge carriers in the n-type semiconductor region of the high carbon AMS specimens compared to the CTP case implies a more disordered outer layer, predominantly composed of iron and nickel oxides. Furthermore, the Mott-Schottky plot demonstrates an upward shift, indicating a lower capacitive behaviour of the native oxide layer and, consequently, a higher resistance for the case of low carbon alloy. It should be noted that the capacitance observed, as previously discussed, is associated with the space charge capacitance of the layer, which contributes more significantly than the double layer capacitance.

The summary of the obtained charge carrier densities from the analysis of the slope of the Mott-Schottky curves is presented in Table 9. It is noteworthy that the alteration in the slope of the n-region is thought to be associated with the applied potential and the status of the formation of nickel and iron oxides-hydroxides, as well as the passive-transpassive state of the surface interacting with the solution, a phenomenon also documented by Cheng et al [72].

Table 9. Charge carrier densities obtained from Mott-Schottky Analysis on AMS and CTP alloy 718 with a standard deviation of 3% based on multiple measurements.

AMS				CTP			
N_a	N_{d1}	N_{d2}	N_{d3}	N_a	N_{d1}	N_{d2}	N_{d3}
7.87E+19	6.49E+19	2.71E+21	3.34E+19	7.57E+19	5.92E+19	1.17E+21	2.63E+19

To examine the characteristics of the passive layer on the surface of both alloys, EIS polarization measurements were carried out at OCP, with a value of -217 mV for low carbon and -197 mV for high carbon specimens, relative to SCE. Illustrated in Figure 10b, the Bode plots exhibit dominant capacitive behaviour at medium to low frequencies, which is mostly related to the passive oxide layer effect with its associated charge transfer resistance against faradaic reactions. Moreover, from Figure 10b, a single time constant is observed for both alloys, signifying capacitive behaviour correlated with passive layer characteristics. The electrochemical impedance measured at higher frequencies is generally associated with the resistance of the electrolyte in contact with the electrode and was nearly identical for both alloys.

To gain further insights into the EIS results, an equivalent circuit was fitted (see inset of Figure 10b), comprising R_e as the solution resistance in parallel with R_t and constant phase element (CPE) of Q as indicators of passive layer behaviour. The fitted data, along with the corresponding error, is summarized in Table 10. As evident, the alloy with lower carbon content exhibited lower capacitance and higher resistance compared to its high-carbon counterpart. This observation suggests that the native oxide layer formed on the surface of the high-carbon L-PBF 718 alloy provides less protection compared to those formed on its low-carbon counterpart. It is important to note that R_t and Q represent the combined effect of the double layer in the close vicinity of the surface and the native oxide layer present. Given that the resistance and capacitance of the double layer are considerably lower compared to those of the native oxide layer, it can be asserted that the fitted values are indicative of the passive layer characteristics.

Table 10. Fitted values for the equivalent electrical circuit for the EIS measurements with a standard deviation of 5% based on multiple experiments performed.

	CTP		AMS	
Parameter	Value	± Error	Value	± Error
R_t (Ω)	1.17E+08	8.14E+07	1.18E+07	1.10E+06
R_e (Ω)	16.6897	0.135	17.1442	0.1391
Q ($F.s^{-(1-\alpha)}$)	4.24E-06	2.19E-08	5.69E-06	2.93E-08
alpha	0.917	9.43E-04	0.9221	9.72E-04

3.6. Stress assisted corrosion behaviour

To elucidate the resistance of the native oxide layer of L-PBF processed alloy 718 with varying carbon content to stress-assisted localized corrosion attack, potentiostatic and galvanostatic polarization tests were conducted under stress-loading conditions. The current and potential response recorded during these experiments are shown in Figure 11. Potentiostatic polarization experiments were conducted at a potential value 10% lower than the breakdown potential determined from potentiodynamic polarization measurements for each specimen. As depicted in Figure 11a, the current density for both alloys approached almost zero during the polarization experiment, indicating the resistance of the native oxide layer to charge transfer. After almost 1500 seconds, a sudden increase in current density was observed for both cases. However, the specimen with lower carbon content was able to offset the charge and reduce the current density to a lower level for the remainder of the polarization experiment, while the specimen with higher carbon content exhibited a substantial increase in current density. This observation suggests a possible leakage of current through the native oxide layer, attributed to local breakdown of the native oxide layer and localized corrosion attack.

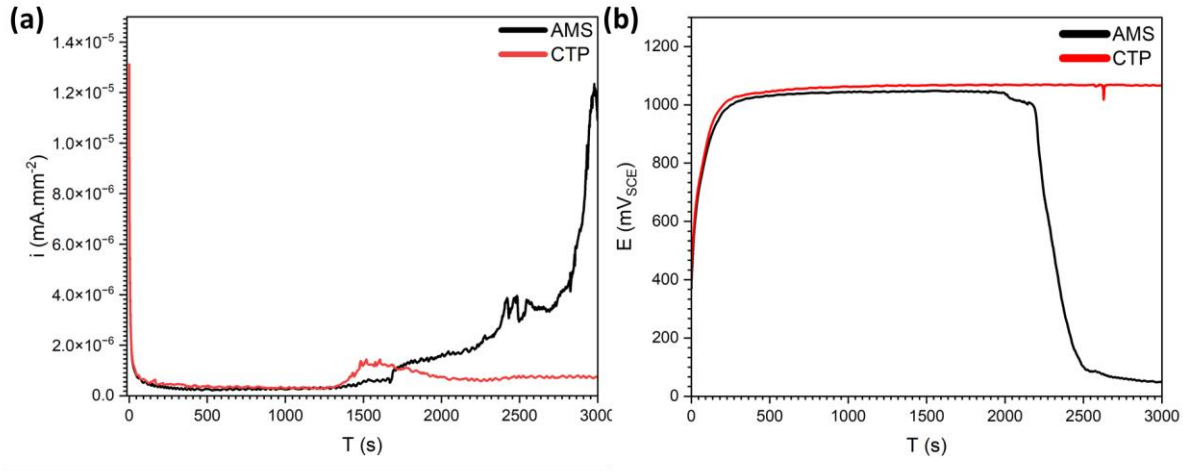

Figure 11. Polarization results for (a) potentiostatic under constant potential, and (b) galvanostatic under constant current density carried out in 3.5 wt.% NaCl solution for the AMS and CTP alloy 718.

Additionally, galvanostatic polarization measurements were conducted on both specimens at a current density corresponding to the passive layer breakdown of 2.7E-4 $mA.mm^{-2}$, as determined from potentiodynamic polarization measurements. This experimental condition takes into account both the mechanical and corrosion limits of the material simultaneously, providing further insights into the longevity of the native oxide layer under critical conditions. As shown in Figure 11b, the potential increases with a similar trend for both cases and stabilizes at around 1000 mV_{SCE}. This gradual increase in potential over the course of polarization is attributed to the formation of the native oxide layer acting as a barrier against the free movement of ions. After approximately 2000 seconds, a sudden discharge occurs for the alloy with higher carbon content, causing a significant drop in potential to much lower values compared to the low carbon alloy. However, a sudden spike in potential is also detected for the low carbon alloy at 2600 seconds, returning back to the previous high value. This observation indicates a localized corrosion attack and discharge occurring on the native oxide layer, with the possibility of repassivation for the case of the low carbon alloy.

3.7. Surface analysis after polarization

Surface analysis was conducted after galvanostatic polarization experiments to gain deeper insights into the morphology of surface attacks and the potential initiation of surface passive layer cracking under corrosion polarization conditions. Figure 12 illustrates the presence of corrosion attacks for both samples, characterized by selective attack at cell interiors while preserving the integrity of cell boundaries.

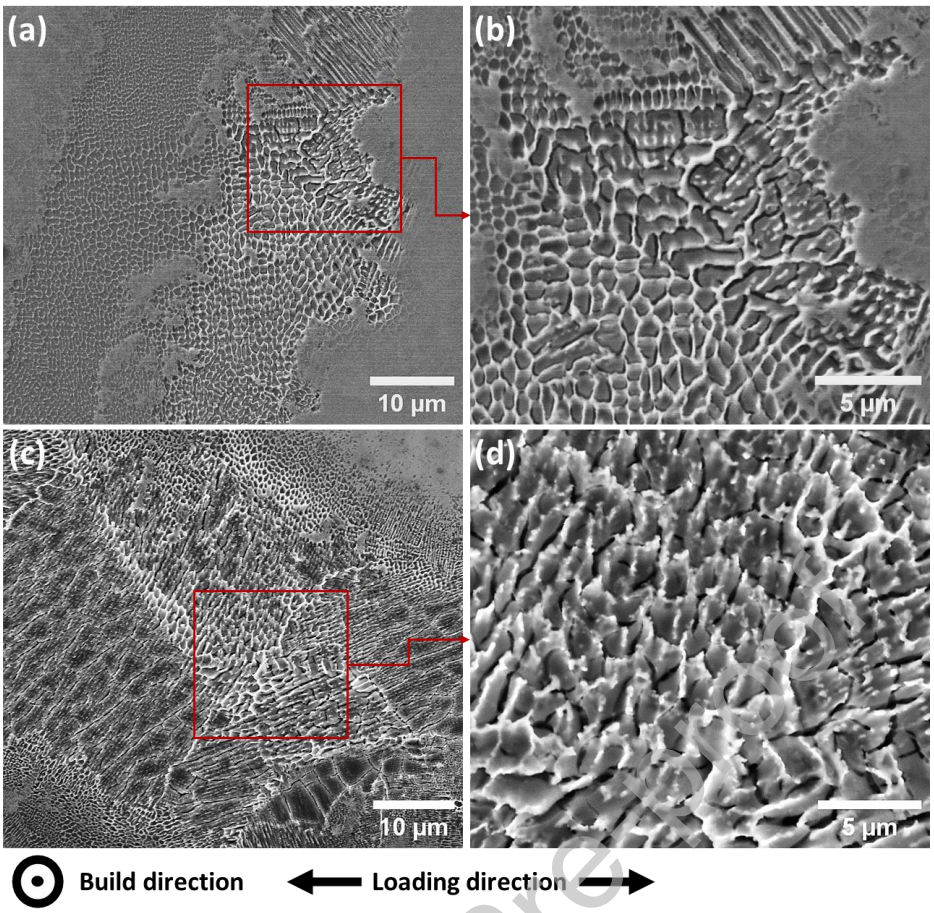

Figure 12. SEM analysis of the surface after galvanostatic polarization experiment under constant current density of 6.5E-05 mA.mm^{-2} for both (a), (b) low carbon CTP alloy, and (c), (d) high carbon AMS alloy.

Notably, the high carbon alloy exhibited a significantly more severe attack, indicating pronounced selective corrosion at the cellular level. Furthermore, observable signs of cracks on the passive layer are present for the alloy with lower carbon content (Figure 12a, b), while the high carbon counterpart displays a higher number and increased severity of cracks (Figure 12c, d). In both instances, cracks are predominantly situated adjacent to cell boundaries, implying a heightened vulnerability of such sites to the initiation of surface cracks. In previous studies by the authors [29,30,57,58], the mechanism underlying the initiation of surface cracks was extensively elucidated. It was attributed to the synergistic effect of the high dislocation density near cell boundaries and the formation of a coupled environment between the cell interior and the decorated cell boundaries. Interested readers are encouraged to delve into the comprehensive explanation of these underlying mechanisms in the authors' earlier investigations.

It is essential to emphasize that the current investigation specifically targets crack initiation at a local site using the microcapillary test method with a 500 µm diameter under constant tensile straining conditions. These surface cracks may act as initiation sites for potential propagation under sustained tensile loading or alternative loading methods. The blunting of the crack tip could occur after a certain

duration, and it is pertinent to note that crack propagation is beyond the current investigation's scope. Nevertheless, the most crucial observation stemming from the corrosion surface analysis post-polarization tests underscores a significantly higher corrosion attack on the native oxide layer of the high carbon alloy when compared to its low carbon counterpart.

4. Discussion

The electrochemical results indicated that alloy 718 processed via L-PBF with reduced carbon content exhibits superior corrosion resistance compared to the standard counterpart, both as-built and under tensile straining, which induces surface corrosion-assisted cracking. To comprehensively reveal the underlying mechanisms, understanding the interplay between carbon and the microstructure under the rapid cooling rates inherent in the L-PBF process is crucial.

Ni-Fe-Cr-based alloys feature an austenitic FCC nickel matrix. This structure is renowned for its high capacity to dissolve alloying elements effectively [73]. Conversely, due to their significantly smaller size, carbon atoms dissolve interstitially in austenite, occupying spaces between the larger substitutional atoms within the FCC lattice. While the inherently low room-temperature solubility of carbon in FCC structures, due to unfavourable lattice packing, typically promotes carbide formation during solidification [74], the rapid cooling rates associated with the L-PBF process can significantly enhance carbon entrapment, potentially impacting material properties at the submicron level. Here, a seemingly minor carbon content change of 0.04% within the FCC nickel matrix could hold significant consequences at submicron level (since maximum solubility is less than 0.1%) [75]. The insertion of carbon atoms into interstitial sites creates local strain energy. Due to the size difference, this distorts the surrounding lattice and alters the FCC structure's parameters [76]. Additionally, these interstitial carbon atoms impede dislocation movement by acting as energy barriers that hinder shearing through atomic planes [77,78]. Consequently, as carbon content increases, dislocation density rises, leading to enhanced resistance to plastic deformation and improved material strength. Furthermore, interstitial carbon atoms can hinder dislocation motion by pinning them at specific lattice sites [77,79,80]. These interstitial points impede dislocation propagation, leading to the formation of dislocation tangles or clusters, further contributing to the increase in dislocation density. EBSD-KAM and TEM analysis, as shown in Figure 4, Figure 6, and Table 3 confirms this by revealing a greater density of entangled dislocations in the specimen with higher carbon content. It is important to note that, as suggested by TEM analysis, the high cooling rates associated with the L-PBF method significantly reduce carbide particle formation.

It is well recognized that the oxidation of multi-component alloys, such as stainless steels and nickel-based alloys, involves a complex interplay between thermodynamic stability and atomic diffusion. Chromium, owing to its high affinity for oxygen and thermodynamically favourable reaction, preferentially forms a continuous, adherent Cr_2O_3 layer as a protective barrier against further

oxidation [55]. Subsequent oxidation of elements like nickel and iron occurs primarily above the Cr_2O_3 layer, given their slower diffusion rates and less thermodynamically favourable kinetics through the established Cr-enriched oxide. The formation of a bilayer structure, with an inner Cr_2O_3 layer and an outer layer predominantly composed of nickel and iron oxides/hydroxides, is a consequence of these differential oxidation kinetics [55,63–65,81,82]. This process is influenced by factors such as oxygen partial pressure, temperature, and alloy composition [55,81].

Furthermore, the Gibbs free energy (ΔG) governing oxide formation dictates the stability and feasibility of oxide generation under standard conditions. Referring to Ellingham diagrams [83,84], which depict the standard ΔG of oxide formation across temperatures, reveals a notably negative ΔG for chromium(III) oxide (Cr_2O_3), approximately -1135 kJ mol^{-1} at 25 °C. This indicates a thermodynamically favourable environment for chromium oxide formation. Consequently, an inner layer enriched in chromium oxides forms adjacent to the base metal, a well-documented phenomenon in Ni-Cr-based alloys and austenitic stainless steels [72,85–87]. This chromium-rich native oxide layer, critical for corrosion resistance in Ni-Cr-based materials, significantly hinders the oxidation of elements like nickel and iron. At higher potentials, the point defect model [88,89] suggests the ejection of nickel and iron from the chromium oxide layer at the metal/passive layer interface. The ΔG values for both nickel and iron oxides are approximately -244 and -272 kJ mol^{-1}, respectively, signifying a lower tendency for oxide formation compared to chromium oxides.

Furthermore, Lozano-Perez et al. [90] employed atomistic analysis to elucidate the formation sequence of oxides in simulated nuclear reactor conditions. Their findings revealed that chromium oxides form preferentially due to favourable thermodynamics (negative ΔG) during oxygen diffusion, displacing nickel and iron. Higher dislocation density further promotes oxidation processes. Furthermore, Hakiki et al. [64,70] investigated the influence of temperature on the native oxide layer's semiconducting behaviour in which the diffusion of elements is facilitated significantly. Interestingly, they observed minimal changes in charge carrier density within the inner chromium oxide layer (p-type region) with temperature variation. Conversely, the charge carrier density in the outer nickel and iron oxides (n-type region) displayed a significant increase with rising temperature. This suggests that chromium oxidation is primarily driven by thermodynamics, whereas the behaviour of iron and nickel oxides is more sensitive to the material's internal energy state.

This observation aligns with the XPS analysis (Table 6, Table 8, and Figure 10a) showing a consistent chromium oxide content across samples with varying carbon content. The p-type region slope in Mott-Schottky analysis (Figure 10a) further supports this notion, as it inversely correlates with dopant density, indicating minimal influence of carbon content on chromium oxide formation kinetics. Conversely, Mott-Schottky analysis revealed a clear difference in dopant densities within the n-type region (linked to nickel and iron oxides) between the two alloys. This aligns with the lower ΔG values

for Fe and Ni oxidation compared to chromium, as reported previously [59,60,64,70]. Consequently, the local energy state plays a more significant role in the oxidation kinetics of iron and nickel, as confirmed by the enhanced diffusion observed in regions with higher dislocation density [90]. This accelerated diffusion leads to a higher density of defects within the outer oxide layer, which manifests as a significant increase in charge carrier density and a steeper slope in the n-type region of the Mott-Schottky plot.

Thus, it could be stated that an increase in material's energy state, established here as a higher density of entangled dislocations due to the presence of interstitial carbon atoms and higher KAM values from EBSD analysis, facilitates the oxidation of nickel and iron. This occurs by overcoming the passivation effect of the native chromium oxide layer on the surface. Consequently, a material with a higher energy state forms a thicker oxide layer composed of other elements (such as nickel and iron in this investigation) compared to a lower energy material. This enhanced oxidation susceptibility can be attributed to the presence of fast diffusion paths created by the increased dislocation density, as also suggested by Lozano-Perez [90].

It is widely acknowledged that the corrosion resistance of passive materials correlates inversely with the density of charge carriers [59–67,69–71,91], a trend consistent with the findings of the present study. Therefore, although the specimen with higher carbon content presents a higher amount of iron and nickel oxides on the surface (and possibly an overall thicker oxide layer), this outer oxide film is enriched in dopants sites and defects (in agreement with the higher film capacitance calculated from the EIS and Mott-Schottky analysis), which increases its susceptibility to pitting corrosion attack.

Electrochemical and surface analysis results confirmed significant alterations in the thickness of Fe and Ni oxides for the investigated alloys. However, other elements like Mo and Nb exhibited minimal variations and did not mirror the trends observed for Fe and Ni. However, in the current investigation Ni, Fe, and Cr oxides/hydroxides were primarily studied, reflecting the historical understanding of their role in forming a bilayer oxide structure: an inner Cr-rich oxide layer and an outer layer enriched with Ni and Fe oxides/hydroxides. Further investigation is necessary to elucidate the mechanisms of the influence of carbon content variations on the oxidation behaviour of all elements, including Nb and Mo.

Regarding the polarization experiments under tensile strain condition, the observed increase in potential during galvanostatic polarization experiments indicates an enhanced resistance to ion transport across the passive layer. This phenomenon is consistent with Ohm's law, where a constant current density necessitates a higher potential difference to overcome increased resistance. For passive materials, a dynamic equilibrium exists between the formation and dissolution of the protective oxide film [71,88,89]. While a stable passive layer is characterized by a significantly slower dissolution rate compared to film formation, anodic polarization can disrupt this balance, promoting dissolution and

leading to passive layer breakdown. Consequently, an initial potential rise reflects the formation of a protective passive film, while a subsequent potential drop corresponds to localized breakdown and a transition to a more active state with facilitated ion transport. Despite these distinct potential regimes, both stages involve predominantly anodic reactions, with the critical distinction being the integrity of the passive film.

Previous investigations by the authors [29,30] have established that crack initiation originates from the selective dissolution of cell matrix, facilitated by galvanic coupling between the matrix and cell boundary phases. The presence of a high dislocation density adjacent to cell boundaries, as revealed by microstructural analysis shown in Figure 12, has been associated with crack initiation. This high dislocation density increases susceptibility to localized corrosion by creating regions with a higher concentration of point defects. According to the point defect model [88], regions with higher energy levels exhibit a greater density of point defects, which enhances the kinetics of the corrosion process, leading to highly localized attacks. Consequently, the passive film is more prone to breakdown in these areas. Thus, the combination of high energy levels adjacent to cell boundaries and the inherent mismatch between constituent phases further promotes crack initiation in which higher dislocation density is directly correlated with observed higher susceptibility to surface cracking.

Another point worth discussing concerns the relation between the SKPFM results and the pitting corrosion susceptibility of the specimens. In the current investigation, a higher potential was measured for the AMS alloy, with higher carbon content, compared to the CTP alloy. Nevertheless, despite the higher potential measured, the AMS alloy presented a higher susceptibility to pitting corrosion attack than the CTP alloy. When utilizing the SKPFM technique, researchers often associate higher potential values with higher nobility, and therefore a higher resistance to corrosion. However, a recent work demonstrated that this correlation is not straightforward [34]. Unusual correlations have been reported in previous studies between SKPFM data and corrosion susceptibility of different phases in Ni-based alloys [92] and other materials [93,94]. The susceptibility of a metal to corrosion, although related to the work function/potential, is also strongly dependent on the nature of the surrounding electrolyte and the reactions that can take place at the metal-oxide/electrolyte interface. The relatively higher potential measured on the AMS sample compared to the CTP specimen can be the result of a thicker oxide layer, as confirmed by the XPS measurements (thicker Fe and Ni oxide outer layer). However, in light of the findings from this study, it becomes evident that a nobler CPD value does not necessarily indicate better corrosion performance. Although the thickness, and consequently the measured Volta potential of the AMS sample, is higher than that of the CTP specimen, this thicker outer layer (enriched in Fe and Ni oxides) is more defective than the constant Cr oxide-rich layer. Thus, increasing the susceptibility of the material to pitting corrosion initiation.

Conclusion

In conclusion, this study delved into the complex mechanisms governing the impact of minor variations in carbon content on the corrosion behaviour of laser powder bed fusion (L-PBF) processed Ni-Fe-Cr based alloy 718. Unlike conventional alloys, where the effect of carbon content on corrosion characteristics is typically attributed to the formation of carbide phases, the current investigation revealed a different mechanism for additively manufactured materials. In these materials, characterized by extremely high cooling rates during solidification, higher amounts of carbon are dissolved in the metal matrix. It was found that lower carbon content resulted in better corrosion performance. The key findings of this study can be summarized as follows:

- From extensive TEM analysis it could be confirmed that carbon in L-PBF-processed alloy 718 primarily exists as interstitial atoms within the FCC sublattice, rather than forming large carbide particles due to the extreme thermal cycles and cooling rates inherent to the L-PBF process. These carbon atoms within the metal matrix caused an increase in dislocation densities, which consequently stimulated a higher oxidation of iron and nickel on the outer layer of the native oxide film.
- Although higher amounts of iron and nickel oxides were formed on the surface of the alloy with higher carbon content, the amount of chromium oxide showed less sensitivity to alterations in carbon content.
- A relatively thicker iron and nickel outer oxide layer on the higher carbon content alloy was characterized by an elevated density of donor charge carriers, which increased the susceptibility of the alloy to pitting corrosion attack.

These findings shed light on the intricate interplay between carbon content, dislocation density, and corrosion behaviour in L-PBF processed Ni-Cr-Fe-based alloy 718.

Data availability

The raw data required to reproduce these findings can be made available upon reasonable request.

Acknowledgement

This work was supported by the University of Padova, Department of Industrial Engineering, and Department of Materials and Chemistry, Research Group Electrochemical and Surface Engineering, Vrije Universiteit Brussel (VUB).

References

[1] A. Bandyopadhyay, S. Bose, Additive manufacturing, CRC press, 2019.

[2] D. Herzog, V. Seyda, E. Wycisk, C. Emmelmann, Additive manufacturing of metals, Acta Mater. 117 (2016) 371–392. https://doi.org/10.1016/j.actamat.2016.07.019.

[3] K. Moussaoui, W. Rubio, M. Mousseigne, T. Sultan, F. Rezai, Effects of Selective Laser Melting additive manufacturing parameters of Inconel 718 on porosity, microstructure and mechanical properties, Mater. Sci. Eng. A 735 (2018) 182–190.

[4] Q. Jia, D. Gu, Selective laser melting additive manufacturing of Inconel 718 superalloy parts: Densification, microstructure and properties, J. Alloys Compd. 585 (2014) 713–721.

[5] D.F. Paulonis, J.M. Oblak, D.S. Duvall, Precipitation in Nickel-base Alloy 718., Pratt and Whitney Aircraft, Middletown, Conn., 1969.

[6] M.K. Miller, S.S. Babu, M.G. Burke, Intragranular precipitation in alloy 718, Mater. Sci. Eng. A 270 (1999) 14–18.

[7] G. Muralidharan, R.G. Thompson, S.D. Walck, Analysis of precipitation in cast alloy 718, Ultramicroscopy 29 (1989) 277–283.

[8] F. Theska, K. Nomoto, F. Godor, B. Oberwinkler, A. Stanojevic, S.P. Ringer, S. Primig, On the early stages of precipitation during direct ageing of Alloy 718, Acta Mater. 188 (2020) 492–503.

[9] J.F. Radavich, The physical metallurgy of cast and wrought alloy 718, Superalloy 718 (1989) 229–240.

[10] M.T. Miglin, Microstructure and stress corrosion resistance of alloys X-750, 718, and A-286 in LWR environments, Electric Power Research Inst., Palo Alto, CA (USA); Babcock and Wilcox Co …, 1989.

[11] M. Wang, M. Song, G.S. Was, J.L. Nelson, The roles of thermal mechanical treatment and δ phase in the stress corrosion cracking of alloy 718 in primary water, Corros. Sci. 160 (2019) 108168. https://doi.org/10.1016/j.corsci.2019.108168.

[12] M. Wang, M. Song, G.S. Was, L. Nelson, Stress Corrosion Cracking Behavior of Alloy 718 Subjected to Various Thermal Mechanical Treatments in Primary Water, in: J.H. Jackson, D. Paraventi, M. Wright (Eds.), Proc. 18th Int. Conf. Environ. Degrad. Mater. Nucl. Power Syst. – Water React., Springer International Publishing, Cham, 2019: pp. 293–305. https://doi.org/10.1007/978-3-030-04639-2_19.

[13] N.K. Sheth, J.A. Manriquez, J.M. Sanchez, M.T. Miglin, J.L. Nelson, Delta (Ni 3 Nb) and IGSCC degradation in alloy 718 and derivatives, in: Proc. Sixth Int. Symp. Environ. Degrad. Mater. Nucl. Power Syst.-Water React., 1993.

[14] H. Zheng, X.N. Ye, J.D. Li, L.Z. Jiang, Z.Y. Liu, G.D. Wang, B.S. Wang, Effect of carbon content on microstructure and mechanical properties of hot-rolled low carbon 12Cr–Ni stainless steel, Mater. Sci. Eng. A 527 (2010) 7407–7412. https://doi.org/10.1016/j.msea.2010.08.023.

[15] M.G. Barker, S.A. Frankham, The effects of carbon and nitrogen on the corrosion resistance of type 316 stainless steel to liquid lithium, J. Nucl. Mater. 107 (1982) 218–221. https://doi.org/10.1016/0022-3115(82)90422-6.

[16] A.J. Sedriks, Corrosion of stainless steels, John Wiley & Sons, 1996.

[17] A.N. Isfahany, H. Saghafian, G. Borhani, The effect of heat treatment on mechanical properties and corrosion behavior of AISI420 martensitic stainless steel, J. Alloys Compd. 509 (2011) 3931–3936. https://doi.org/10.1016/j.jallcom.2010.12.174.

[18] E.A. Trillo, L.E. Murr, Effects of carbon content, deformation, and interfacial energetics on carbide precipitation and corrosion sensitization in 304 stainless steel, Acta Mater. 47 (1998) 235–245. https://doi.org/10.1016/S1359-6454(98)00322-X.

[19] M.M. Attallah, R. Jennings, X. Wang, L.N. Carter, Additive manufacturing of Ni-based superalloys: The outstanding issues, MRS Bull. 41 (2016) 758–764.

[20] J.S. Zuback, P. Moradifar, Z. Khayat, N. Alem, T.A. Palmer, Impact of chemical composition on precipitate morphology in an additively manufactured nickel base superalloy, J. Alloys Compd. 798 (2019) 446–457.

[21] M. Shahwaz, P. Nath, I. Sen, A critical review on the microstructure and mechanical properties correlation of additively manufactured nickel-based superalloys, J. Alloys Compd. 907 (2022) 164530.

[22] W.M. Tucho, V. Hansen, Studies of Post-Fabrication Heat Treatment of L-PBF-Inconel 718: Effects of Hold Time on Microstructure, Annealing Twins, and Hardness, Metals 11 (2021) 266. https://doi.org/10.3390/met11020266.
[23] W.M. Tucho, V. Hansen, Characterization of SLM-fabricated Inconel 718 after solid solution and precipitation hardening heat treatments, J. Mater. Sci. 54 (2019) 823–839. https://doi.org/10.1007/s10853-018-2851-x.
[24] W.M. Tucho, P. Cuvillier, A. Sjolyst-Kverneland, V. Hansen, Microstructure and hardness studies of Inconel 718 manufactured by selective laser melting before and after solution heat treatment, Mater. Sci. Eng. A 689 (2017) 220–232. https://doi.org/10.1016/j.msea.2017.02.062.
[25] M. Laleh, E. Sadeghi, R.I. Revilla, Q. Chao, N. Haghdadi, A.E. Hughes, W. Xu, I. De Graeve, M. Qian, I. Gibson, M.Y. Tan, Heat treatment for metal additive manufacturing, Prog. Mater. Sci. 133 (2023) 101051. https://doi.org/10.1016/j.pmatsci.2022.101051.
[26] S. Luo, W. Huang, H. Yang, J. Yang, Z. Wang, X. Zeng, Microstructural evolution and corrosion behaviors of Inconel 718 alloy produced by selective laser melting following different heat treatments, Addit. Manuf. 30 (2019) 100875. https://doi.org/10.1016/j.addma.2019.100875.
[27] B. Zhang, M. Xiu, Y.T. Tan, J. Wei, P. Wang, Pitting corrosion of SLM Inconel 718 sample under surface and heat treatments, Appl. Surf. Sci. 490 (2019) 556–567. https://doi.org/10.1016/j.apsusc.2019.06.043.
[28] D. Du, A. Dong, D. Shu, G. Zhu, B. Sun, X. Li, E. Lavernia, Influence of build orientation on microstructure, mechanical and corrosion behavior of Inconel 718 processed by selective laser melting, Mater. Sci. Eng. A 760 (2019) 469–480. https://doi.org/10.1016/j.msea.2019.05.013.
[29] A. Yazdanpanah, R.I. Revilla, M. Franceschi, A. Fabrizi, S. Khademzadeh, M. Khodabakhshi, I. De Graeve, M. Dabalà, Unveiling the impact of laser power variations on microstructure, corrosion, and stress-assisted surface crack initiation in laser powder bed fusion-processed Ni-Fe-Cr alloy 718, Electrochimica Acta 476 (2024) 143723. https://doi.org/10.1016/j.electacta.2023.143723.
[30] A. Yazdanpanah, M. Franceschi, R.I. Revilla, S. Khademzadeh, I. De Graeve, M. Dabalà, Revealing the stress corrosion cracking initiation mechanism of alloy 718 prepared by laser powder bed fusion assessed by microcapillary method, Corros. Sci. 208 (2022) 110642. https://doi.org/10.1016/j.corsci.2022.110642.
[31] E.L. Hall, C.L. Briant, Chromium depletion in the vicinity of carbides in sensitized austenitic stainless steels, Metall. Trans. A 15 (1984) 793–811. https://doi.org/10.1007/BF02644554.
[32] W. Zhou, Y. Tian, Q. Tan, S. Qiao, H. Luo, G. Zhu, D. Shu, B. Sun, Effect of carbon content on the microstructure, tensile properties and cracking susceptibility of IN738 superalloy processed by laser powder bed fusion, Addit. Manuf. 58 (2022) 103016.
[33] J. Zheng, S. Chen, L. Jiang, X.-X. Ye, C. Xu, Z. Li, Effect of carbon content on the microstructure and mechanical properties of NiCrFe-7A alloys synthesized by wire arc additive manufacturing, Mater. Sci. Eng. A 842 (2022) 142925. https://doi.org/10.1016/j.msea.2022.142925.
[34] R.I. Revilla, Methods—On the Application of Ambient Scanning Kelvin Probe Force Microscopy to Understand Micro-Galvanic Corrosion Phenomena: Interpretation and Challenges, J. Electrochem. Soc. 170 (2023) 011501. https://doi.org/10.1149/1945-7111/acafab.
[35] D. Briggs, Practical surface analysis, Auger X-Ray Photoelectron Spectrosc. 607 (1995).
[36] D.A. Shirley, High-resolution X-ray photoemission spectrum of the valence bands of gold, Phys. Rev. B 5 (1972) 4709.
[37] Q. Teng, S. Li, Q. Wei, Y. Shi, Investigation on the influence of heat treatment on Inconel 718 fabricated by selective laser melting: Microstructure and high temperature tensile property, J. Manuf. Process. 61 (2021) 35–45. https://doi.org/10.1016/j.jmapro.2020.11.002.
[38] P. Liu, J. Hu, S. Sun, K. Feng, Y. Zhang, M. Cao, Microstructural evolution and phase transformation of Inconel 718 alloys fabricated by selective laser melting under different heat treatment, J. Manuf. Process. 39 (2019) 226–232. https://doi.org/10.1016/j.jmapro.2019.02.029.
[39] A. Yazdanpanah, M. Franceschi, P. Rebesan, M. Dabalà, Correlation of Lack of Fusion Pores with Stress Corrosion Cracking Susceptibility of L-PBF 316L: Effect of Surface Residual Stresses, Materials 15 (2022) 7151. https://doi.org/10.3390/ma15207151.

[40] R.I. Revilla, H. Terryn, I. De Graeve, On the use of SKPFM for in situ studies of the repassivation of the native oxide film on aluminium in air, Electrochem. Commun. 93 (2018) 162–165. https://doi.org/10.1016/j.elecom.2018.07.010.
[41] L. Ramqvist, K. Hamrin, G. Johansson, A. Fahlman, C. Nordling, Charge transfer in transition metal carbides and related compounds studied by ESCA, J. Phys. Chem. Solids 30 (1969) 1835–1847. https://doi.org/10.1016/0022-3697(69)90252-2.
[42] G.D.C.F.A. Chemie, Fresenius' Zeitschrift für analytische Chemie, Springer-Verlag; München, 1963.
[43] G. Pagot, M.C. Cassani, F. Gambassi, B. Ballarin, D. Nanni, M. Coi, D. Barreca, E. Boanini, V. Di Noto, Propargyl carbamate-functionalized Cu(II)-metal organic framework after reaction with chloroauric acid: An x-ray photoelectron spectroscopy data record, Surf. Sci. Spectra 29 (2022) 024007. https://doi.org/10.1116/6.0001950.
[44] G. Pagot, M. Benedet, C. Maccato, D. Barreca, V. Di Noto, XPS study of NiO thin films obtained by chemical vapor deposition, Surf. Sci. Spectra 30 (2023) 024028. https://doi.org/10.1116/6.0003008.
[45] C. Triolo, S. Schweidler, L. Lin, G. Pagot, V.D. Noto, B. Breitung, S. Santangelo, Evaluation of electrospun spinel-type high-entropy (Cr0.2Mn0.2Fe0.2Co0.2Ni0.2)3O4, (Cr0.2Mn0.2Fe0.2Co0.2Zn0.2)3O4 and (Cr0.2Mn0.2Fe0.2Ni0.2Zn0.2)3O4 oxide nanofibers as electrocatalysts for oxygen evolution in alkaline medium, Energy Adv. 2 (2023) 667–678. https://doi.org/10.1039/D3YA00062A.
[46] C. Triolo, K. Moulaee, A. Ponti, G. Pagot, V. Di Noto, N. Pinna, G. Neri, S. Santangelo, Spinel-Structured High-Entropy Oxide Nanofibers as Electrocatalysts for Oxygen Evolution in Alkaline Solution: Effect of Metal Combination and Calcination Temperature, Adv. Funct. Mater. 34 (2024) 2306375. https://doi.org/10.1002/adfm.202306375.
[47] C. Triolo, M. Maisuradze, M. Li, Y. Liu, A. Ponti, G. Pagot, V. Di Noto, G. Aquilanti, N. Pinna, M. Giorgetti, S. Santangelo, Charge Storage Mechanism in Electrospun Spinel-Structured High-Entropy (Mn0.2Fe0.2Co0.2Ni0.2Zn0.2)3O4 Oxide Nanofibers as Anode Material for Li-Ion Batteries, Small 19 (2023) 2304585. https://doi.org/10.1002/smll.202304585.
[48] V.I. Nefedov, Y.V. Salyn, G. Leonhardt, R. Scheibe, A comparison of different spectrometers and charge corrections used in X-ray photoelectron spectroscopy, J. Electron Spectrosc. Relat. Phenom. 10 (1977) 121–124.
[49] D.D. Hawn, B.M. DeKoven, Deconvolution as a correction for photoelectron inelastic energy losses in the core level XPS spectra of iron oxides, Surf. Interface Anal. 10 (1987) 63–74.
[50] N.S. McIntyre, M.G. Cook, X-ray photoelectron studies on some oxides and hydroxides of cobalt, nickel, and copper, Anal. Chem. 47 (1975) 2208–2213.
[51] R.P. Furstenau, G. McDougall, M.A. Langell, Initial stages of hydrogen reduction of NiO (100), Surf. Sci. 150 (1985) 55–79.
[52] N. Uekawa, K. Kaneko, Dopant reduction in p-type oxide films upon oxygen absorption, J. Phys. Chem. 100 (1996) 4193–4198.
[53] D. Shuttleworth, Preparation of metal-polymer dispersions by plasma techniques. An ESCA investigation, J. Phys. Chem. 84 (1980) 1629–1634.
[54] A. Larsson, G. D'Acunto, M. Vorobyova, G. Abbondanza, U. Lienert, Z. Hegedüs, A. Preobrajenski, L.R. Merte, J. Eidhagen, A. Delblanc, J. Pan, E. Lundgren, Thickness and composition of native oxides and near-surface regions of Ni superalloys, J. Alloys Compd. 895 (2022) 162657. https://doi.org/10.1016/j.jallcom.2021.162657.
[55] A. Machet, A. Galtayries, S. Zanna, L. Klein, V. Maurice, P. Jolivet, M. Foucault, P. Combrade, P. Scott, P. Marcus, XPS and STM study of the growth and structure of passive films in high temperature water on a nickel-base alloy, Electrochimica Acta 49 (2004) 3957–3964. https://doi.org/10.1016/j.electacta.2004.04.032.
[56] A. Jablonski, C.J. Powell, NIST Electron Effective-Attenuation-Length Database, PhD Thesis, National Institute of Standards and Technology Gaithersburg, 2011. https://www.nist.gov/document/srd82usersguidev1-3pdf (accessed July 1, 2024).
[57] C. Gasparrini, J.O. Douglas, A. Yazdanpanah, R. Stroud, G. Divitini, M. Dabalà, G.G. Scatigno, S. Pedrazzini, M.R. Wenman, D. Badocco, P. Pastore, N. Terranova, G. Mariano, F. Dacquait, M.D. Palma, R. Villari, P. Sonato, Corrosion of 316L exposed to highly concentrated borated

water used as shield in nuclear fusion experimental reactors cooling circuits, Corros. Sci. 230 (2024) 111902. https://doi.org/10.1016/j.corsci.2024.111902.
[58] A. Yazdanpanah, L. Pezzato, M. Dabalà, Stress corrosion cracking of AISI 304 under chromium variation within the standard limits: Failure analysis implementing microcapillary method, Eng. Fail. Anal. 142 (2022) 106797. https://doi.org/10.1016/j.engfailanal.2022.106797.
[59] N.B. Hakiki, S. Boudin, B. Rondot, M. Da Cunha Belo, The electronic structure of passive films formed on stainless steels, Corros. Sci. 37 (1995) 1809–1822. https://doi.org/10.1016/0010-938X(95)00084-W.
[60] N.E. Hakiki, M.D.C. Belo, A.M.P. Simões, M.G.S. Ferreira, Semiconducting Properties of Passive Films Formed on Stainless Steels: Influence of the Alloying Elements, J. Electrochem. Soc. 145 (1998) 3821. https://doi.org/10.1149/1.1838880.
[61] M. da Cunha Belo, M. Walls, N.E. Hakiki, J. Corset, E. Picquenard, G. Sagon, D. Noël, Composition, structure and properties of the oxide films formed on the stainless steel 316L in a primary type PWR environment, Corros. Sci. 40 (1998) 447–463. https://doi.org/10.1016/S0010-938X(97)00158-3.
[62] M. da Cunha Belo, M. Walls, N.E. Hakiki, J. Corset, E. Picquenard, G. Sagon, D. Noël, Composition, structure and properties of the oxide films formed on the stainless steel 316L in a primary type PWR environment, Corros. Sci. 40 (1998) 447–463. https://doi.org/10.1016/S0010-938X(97)00158-3.
[63] M. Da Cunha Belo, N.E. Hakiki, M.G.S. Ferreira, Semiconducting properties of passive films formed on nickel–base alloys type Alloy 600: influence of the alloying elements, Electrochimica Acta 44 (1999) 2473–2481. https://doi.org/10.1016/S0013-4686(98)00372-7.
[64] N.E. Hakiki, M.F. Montemor, M.G.S. Ferreira, M. da Cunha Belo, Semiconducting properties of thermally grown oxide films on AISI 304 stainless steel, Corros. Sci. 42 (2000) 687–702. https://doi.org/10.1016/S0010-938X(99)00082-7.
[65] M.F. Montemor, M.G.S. Ferreira, N.E. Hakiki, M. Da Cunha Belo, Chemical composition and electronic structure of the oxide films formed on 316L stainless steel and nickel based alloys in high temperature aqueous environments, Corros. Sci. 42 (2000) 1635–1650. https://doi.org/10.1016/S0010-938X(00)00012-3.
[66] M.G.S. Ferreira, N.E. Hakiki, G. Goodlet, S. Faty, A.M.P. Simões, M. Da Cunha Belo, Influence of the temperature of film formation on the electronic structure of oxide films formed on 304 stainless steel, Electrochimica Acta 46 (2001) 3767–3776. https://doi.org/10.1016/S0013-4686(01)00658-2.
[67] R.D. Gryse, W.P. Gomes, F. Cardon, J. Vennik, On the Interpretation of Mott-Schottky Plots Determined at Semiconductor/Electrolyte Systems, J. Electrochem. Soc. 122 (1975) 711. https://doi.org/10.1149/1.2134298.
[68] H. Tsuchiya, S. Fujimoto, Semiconductor properties of passive films formed on sputter-deposited Fe–18Cr alloy thin films with various additive elements, Sci. Technol. Adv. Mater. 5 (2004) 195–200. https://doi.org/10.1016/j.stam.2003.10.014.
[69] S.J. Ahn, H.S. Kwon, Effects of solution temperature on electronic properties of passive film formed on Fe in pH 8.5 borate buffer solution, Electrochimica Acta 49 (2004) 3347–3353. https://doi.org/10.1016/j.electacta.2004.02.043.
[70] N.E. Hakiki, Comparative study of structural and semiconducting properties of passive films and thermally grown oxides on AISI 304 stainless steel, Corros. Sci. 53 (2011) 2688–2699. https://doi.org/10.1016/j.corsci.2011.05.012.
[71] E. Sikora, D.D. Macdonald, Nature of the passive film on nickel, Electrochimica Acta 48 (2002) 69–77. https://doi.org/10.1016/S0013-4686(02)00552-2.
[72] Q. Cheng, X. Zhuang, Quasi-in-situ monitoring of passive film growth of Inconel 718 alloy, Mater. Lett. 335 (2023) 133743. https://doi.org/10.1016/j.matlet.2022.133743.
[73] Phases and Microstructure of Superalloys, (2010). https://doi.org/10.31399/asm.tb.sap.t53000025.
[74] W.L. Mankins, S. Lamb, Nickel and Nickel Alloys, in: ASM Handbook Committee (Ed.), Prop. Sel. Nonferrous Alloys Spec.-Purp. Mater., ASM International, 1990: pp. 428–445. https://doi.org/10.31399/asm.hb.v02.a0001072.

[75] D.E. Jiang, E.A. Carter, Carbon dissolution and diffusion in ferrite and austenite from first principles, Phys. Rev. B 67 (2003) 214103. https://doi.org/10.1103/PhysRevB.67.214103.
[76] J.-E. Ahn, Y.-K. Kim, S. Yang, K.-A. Lee, Interstitial carbon content effect on the microstructure and mechanical properties of additively manufactured NiCoCr medium-entropy alloy, J. Alloys Compd. 918 (2022) 165601. https://doi.org/10.1016/j.jallcom.2022.165601.
[77] G. Bonny, N. Castin, A. Bakaev, A.E. Sand, D. Terentyev, Effects of cascade-induced dislocation structures on the long-term microstructural evolution in tungsten, Comput. Mater. Sci. 181 (2020) 109727. https://doi.org/10.1016/j.commatsci.2020.109727.
[78] A. Bakaev, G. Bonny, N. Castin, D. Terentyev, V.A. Bakaev, Impact of interstitial impurities on the trapping of dislocation loops in tungsten, Sci. Rep. 11 (2021) 12333. https://doi.org/10.1038/s41598-021-91390-1.
[79] A. Cottrell, Dislocations and plastic flow in crystals, Clarendon press, 1956.
[80] J. Svoboda, W. Ecker, V.I. Razumovskiy, G.A. Zickler, F.D. Fischer, Kinetics of interaction of impurity interstitials with dislocations revisited, Prog. Mater. Sci. 101 (2019) 172–206. https://doi.org/10.1016/j.pmatsci.2018.10.001.
[81] Z. Wang, C. Carrière, A. Seyeux, S. Zanna, D. Mercier, P. Marcus, Thermal stability of surface oxides on nickel alloys (NiCr and NiCrMo) investigated by XPS and ToF-SIMS, Appl. Surf. Sci. 576 (2022) 151836. https://doi.org/10.1016/j.apsusc.2021.151836.
[82] Y. Lee, J. Park, W. Yu, W.H. Tanveer, Y.H. Lee, G.Y. Cho, T. Park, C. Zheng, W. Lee, S.W. Cha, Nickel-based bilayer thin-film anodes for low-temperature solid oxide fuel cells, Energy 161 (2018) 1133–1138. https://doi.org/10.1016/j.energy.2018.07.147.
[83] L. Oar-Arteta, T. Wezendonk, X. Sun, F. Kapteijn, J. Gascon, Metal organic frameworks as precursors for the manufacture of advanced catalytic materials, Mater. Chem. Front. 1 (2017) 1709–1745.
[84] R. Das, P. Pachfule, R. Banerjee, P. Poddar, Metal and metal oxide nanoparticle synthesis from metal organic frameworks (MOFs): finding the border of metal and metal oxides, Nanoscale 4 (2012) 591–599. https://doi.org/10.1039/C1NR10944H.
[85] H. Xu, L. Wang, D. Sun, H. Yu, The passive oxide films growth on 316L stainless steel in borate buffer solution measured by real-time spectroscopic ellipsometry, Appl. Surf. Sci. 351 (2015) 367–373. https://doi.org/10.1016/j.apsusc.2015.05.165.
[86] D. Kong, C. Dong, X. Ni, L. Zhang, H. Luo, R. Li, L. Wang, C. Man, X. Li, The passivity of selective laser melted 316L stainless steel, Appl. Surf. Sci. 504 (2020) 144495. https://doi.org/10.1016/j.apsusc.2019.144495.
[87] S. Choudhary, R.G. Kelly, N. Birbilis, On the origin of passive film breakdown and metastable pitting for stainless steel 316L, Corros. Sci. 230 (2024) 111911. https://doi.org/10.1016/j.corsci.2024.111911.
[88] D.D. Macdonald, The history of the Point Defect Model for the passive state: A brief review of film growth aspects, Electrochimica Acta 56 (2011) 1761–1772.
[89] D.D. Macdonald, PassivityÐthe key to our metals-based civilization, Pure Appl Chem 71 (1999) 951–978.
[90] S. Lozano-Perez, D.W. Saxey, T. Yamada, T. Terachi, Atom-probe tomography characterization of the oxidation of stainless steel, Scr. Mater. 62 (2010) 855–858. https://doi.org/10.1016/j.scriptamat.2010.02.021.
[91] B. Lovreček, J. Sefaja, Semiconducting aspects of the passive layer on chromium, Electrochimica Acta 17 (1972) 1151–1155. https://doi.org/10.1016/0013-4686(72)90031-X.
[92] M. Iannuzzi, K.L. Vasanth, G.S. Frankel, Unusual Correlation between SKPFM and Corrosion of Nickel Aluminum Bronzes, J. Electrochem. Soc. 164 (2017) C488. https://doi.org/10.1149/2.0391709jes.
[93] A. Kvryan, K. Livingston, C.M. Efaw, K. Knori, B.J. Jaques, P.H. Davis, D.P. Butt, M.F. Hurley, Microgalvanic corrosion behavior of Cu-Ag active braze alloys investigated with SKPFM, Metals 6 (2016) 91.
[94] C. Liu, R.I. Revilla, X. Li, Z. Jiang, S. Yang, Z. Cui, D. Zhang, H. Terryn, X. Li, New insights into the mechanism of localised corrosion induced by TiN-containing inclusions in high strength low alloy steel, J. Mater. Sci. Technol. 124 (2022) 141–149.

Declaration of interests

☒ The authors declare that they have no known competing financial interests or personal relationships that could have appeared to influence the work reported in this paper.

☐The authors declare the following financial interests/personal relationships which may be considered as potential competing interests: